

ORIGINAL RESEARCH

Open Access



Dual degree branched type-2 fuzzy controller optimized with a hybrid algorithm for frequency regulation in a triple-area power system integrated with renewable sources

Nisha Kumari¹, Pulakraj Aryan² , G. Lloyds Raja^{2*} and Yogendra Arya³

Abstract

The uncertainties associated with multi-area power systems comprising both thermal and distributed renewable generation (DRG) sources such as solar and wind necessitate the use of an efficient load frequency control (LFC) technique. Therefore, a hybrid version of two metaheuristic algorithms (arithmetic optimization and African vulture's optimization algorithm) is developed. It is called the 'arithmetic optimized African vulture's optimization algorithm (AOAVOA)'. This algorithm is used to tune a novel type-2 fuzzy-based proportional–derivative branched with dual degree-of-freedom proportional–integral–derivative controller for the LFC of a three-area hybrid deregulated power system. Thermal, electric vehicle (EV), and DRG sources (including a solar panel and a wind turbine system) are connected in area-1. Area-2 involves thermal and gas-generating units (GUs), while thermal and geothermal units are linked in area-3. Practical restrictions such as thermo-boiler dynamics, thermal-governor dead-band, and generation rate constraints are also considered. The proposed LFC method is compared to other controllers and optimizers to demonstrate its superiority in rejecting step and random load disturbances. By functioning as energy storage elements, EVs and DRG units can enhance dynamic responses during peak demand. As a result, the effect of the aforementioned units on dynamic reactions is also investigated. To validate its effectiveness, the closed-loop system is subjected to robust stability analysis and is compared to various existing control schemes from the literature. It is determined that the suggested AOAVOA improves fitness by 40.20% over the arithmetic optimizer (AO), while frequency regulation is improved by 4.55% over an AO-tuned type-2 fuzzy-based branched controller.

Keywords Load frequency control, Distributed generation, Energy storage devices, Type-2 fuzzy proportional–derivative branched with dual-degree-of-freedom proportional–integral–derivative controller, Hybrid arithmetic optimized African vulture's optimization algorithm

1 Introduction

1.1 Conspectus of load frequency control

Disparities between generation and load-demand introduce power system frequency oscillations which can result in serious consequences. Hence, an efficient load frequency control (LFC) strategy is crucial for eliminating such frequency deviations and maintaining the system dynamics at specified values. Consequently, LFC has attracted a lot of interest over the past 20 years [1–3]. In modern interconnected power networks, even

*Correspondence:

G. Lloyds Raja

lloyd.raja@gmail.com; lloyds.ee@nitp.ac.in

¹ Department of Electrical Engineering, Indian Institute of Technology (Indian School of Mines), Dhanbad, India

² Department of Electrical Engineering, National Institute of Technology, Patna, India

³ Department of Electrical Engineering, J.C. Bose University of Science and Technology, YMCA, Faridabad, Haryana, India

a small disruption in one location can affect the quality of the power in other areas. Since many different control regions are interconnected, these systems are exceedingly complicated, requiring careful planning and effective LFC approaches [4, 5]. Various electricity providers are competing with one another for customers by maximizing their efficiency and lowering the cost of power. The government has therefore designed a restructured regulation scheme known as "deregulation" for these power industries [6]. Under deregulated conditions, when generation firms (GENCOs) do/don't participate, an independent system operator (ISO) is obliged to take care of the LFC. While operating in an open-market, distribution firms (DISCOs) can enter into contracts with any GENCOs of any region based on a disco participation matrix (DPM) to satisfy the load demand [7]. Table 1 provides a brief comparative review of some LFC strategies [1, 4, 8–28].

Conventionally, basic secondary controllers, such as I, PI, PID, and PIDN have been used for LFC [15, 29, 30]. However, these basic controllers have many drawbacks, e.g., long response time, high sensitivity to disturbances, inability to handle complicated systems, etc. Several attempts have been made recently to overcome the aforementioned disadvantages. For instance, to obtain better dynamic performance than single degree-of-freedom (DOF) controllers, two/three DOF controllers are used in [16, 31, 32].

A fractional-order (FO) controller has many evident benefits over an integer-order controller in the frequency regulation domain. An additional DOF, more flexible parameters, and a larger range of slopes are a few of these benefits [33, 34]. As a result, many researchers have used FO controllers for LFC applications [11, 35–37]. Cascade controllers are also implemented to improve closed-loop responses in LFC applications [5, 18, 38], whereas combinations of cascade and two DOF controllers are reported in [22]. Because of the uncertainties involved with renewable energy, modern power systems (PSs) are becoming increasingly complicated and hence require more advanced control strategies. Systems having nonlinearities can be handled more effectively by fuzzy logic-based adaptive controllers [6, 19, 24]. Consequently, fuzzy-logic-aided controllers (FLCs) are frequently adapted in series with PID controllers [39, 40], or cascaded with multi-stage fractional controllers [10, 11, 18, 36]. A combination of FO and type-2 FLC is also reported in [41], while other LFC strategies include the use of a model predictive controller (MPC) [42, 43], linear active disturbance rejection control (LADRC) [44], sliding mode control (SMC) [45, 46], TID controller with filter (TIDN) [34, 47]. To improve frequency stability in an Egyptian power system with high-level renewable penetration, a coordinated control

strategy (CCS) is implemented in [12], whereas CCS has also been used in wind and battery PS [48], wind turbine generators and plug-in type hybrid electric vehicles (PHEVs) [13], and virtual power plants [20].

Several investigators have considered thermal, hydro, and gas units for determining the efficacy of LFC on the system [9, 49–51]. However, very few studies have examined thermo-boiler dynamics (TBD), thermal-governor dead-band (TDB), and generation rate constraint (GRC) nonlinearities [23, 52, 53]. Because of the popularity of renewables in recent times, hybrid PSs involving these sources are considered to study the efficacy of modern LFC strategies [54, 55]. Metaheuristic optimizers don't need the knowledge of the system dynamics, and thus, many such algorithms have been used to find optimal controller gains for LFC applications involving the aforementioned nonlinearities (TBD, TDB and GRC). In addition to those listed in Table 1, the previously used algorithms include particle swarm optimizer (PSO) [56], whale optimizer (WO) [57], SMA [58], Harris hawk optimizer (HHO) [59], teaching–learning based optimizer (TLBO) [60], fruit fly optimization (FFO) [61], hybrid particle swarm optimization-genetic algorithm (PSO-GA) [62], hybrid harmony search and cuckoo optimizer algorithm (HSCOA) [63], hybrid modified grey wolf optimized cuckoo search algorithm (MGWO-CSA) [26], and African vultures optimizer algorithm (AVOA) [64]. Modern PSs need intelligent controllers that are optimized with such metaheuristic optimizers to eliminate frequency deviations and tie-line power variances more effectively.

1.2 Key research gaps and aims

Based on Table 1 and the literature review carried out in Sect. 1.1, the following can be concluded:

1. In the majority of the available literature on restructured three-area, a simple PS is considered [2, 4, 15].
2. The high level of uncertainty connected to the rule base cannot be adequately handled by the type-1 fuzzy system (T1FS). Hence, type-2 fuzzy systems are used to solve this problem [19].
3. When subjected to an overwhelming computational burden, the performance of both type-1 and type-2 fuzzy systems declines. This drawback is eliminated with branched fuzzy structures by providing an extra path for control signals [23, 24]. However, type-2 fuzzy-based branched controllers are yet to be used for three-area PSs.
4. AO and AVOA have shown better convergence than other contemporary algorithms such as PSO, WOA, TLBO, etc. Hence, AO and AVOA are potential candidates for developing a hybrid algorithm [26, 65, 66].

Table 1 A concise overview of published sources on LFC

Author(s)	Controller	Optimizer	Cost function	Control areas	GENCOs	Nonlinearity
Parmar et al. [8]	I	Optimal state feedback		2	Area-1&2: Thermal + Hydro + Gas	None
Shankar et al. [9]	I	OHS	ISE	2	Area-1&2: Thermal + Hydro + Gas	TDB, GRC
Arya and Kumar [10]	FOFPID	BFOA	ISE	2	Area-1&2: Thermal + Hydro	GRC
Arya [11]	FPIDN-FOI	ICA	ISE	2	Area-1&2: Thermal	TD, TDB, GRC
Magdy [12]	PI	PSO	ISE	1	Area-1: Gas, Thermal, Hydraulic, wind and solar	GRC, TDB
Pahasa [13]	MPCs	PSO	IAE	1	Area-1: wind and EV	None
Arya [14]	FFOPI-FOPD	ICA	ISE	3	Area-1, 2&3: Thermal	None
Murali et al. [4]	2-DOF-PIDN	VPLA	ITAE	3	Area-1: EV + Thermal + DRG, Area-2&3: Thermal + Gas	TBD, GRC
Saha and Saikia [1]	IDN-FOPD	WO	ISE	2	Area-1: Thermal + WTS, Area-2: SSGT + Thermal	GRC
Pappachen and Fathima [15]	PI	GA	ITSE	3	Area-1&3: Thermal + SMES, Area-2: Hydro + SMES	GRC
Raj and Shankar [16]	2DOF-PIDN FOID	ISA	ISE	3	Area-1: EV + DRG + Thermal, Area-2: Thermal + Hydro, Area-3: Thermal + Gas	TBD, GRC, and TDB
Prakash et al. [17]	PIDN (1 + FOD)	SSA	ISE	2	Area-1: Thermal + Hydro, Area-2: Thermal + Hydro	None
Nayak et al [18]	FOFPID	SA	ITAE	2	Area-1: WTS + HAE FC + Thermal + Hydro, Area-2: Thermal + Hydro + HAE FC + SP	None
Khadanga et al. [19]	IT2FPID	MEO	ISE	2	Area-1: Hydro + Thermal + DRG, Area-2: Hydro + Thermal + DRG	None
Oshnoei [20]	PID	MOOF	–	1	Area-1: BESSs & HPWHs	None
Sharma et al. [21]	CFPD ^u F-PI	SMA	ISE	2	Area-1&2: Thermal + hydro	None
Murali and Shankar [22]	CC-2-DOF (PI)-PDF	OVPLA	ISE	2	Area-1: DRG + Gas + Thermal + EV, Area-2: Hydro + Thermal	GRC
Aryan and Raja [23]	FFOPI + PIDN	QOEO	ISE	2	Area-1: Thermal + DRG + Geothermal + EV, Area-2: Thermal + Hydro + Bio-gas	TDB, TBD, and GRC
Anand et al. [24]	T2FID + I	AO	ITSE	2	Area-1: Thermal + Hydro + EV + DRG, Area-2: Thermal + Gas	TDB, TBD, and GRC
Padhi et al. [25]	STFPI	QOB Jaya	ITAE	2	Area-1: Thermal + Hydro + WTS, Area-2: Thermal + Hydro + diesel	None
Khadanga et al. [26]	TID	Hybrid MGWO-CSA	ITAE	2	Area-1: SP, Area-2: Thermal + SP	TDB
Celik et al. [27]	PI	SSA	ITAE	2	Area-1: SP + Thermal, Area-2: Thermal + RFB	None

Table 1 (continued)

Author(s)	Controller	Optimizer	Cost function	Control areas	GENCOs	Nonlinearity
Kumari et al. [28]	T2FID + PD	AVOA	ITAE	3	Area-1: EV + DRG + Thermal, Area-2: Thermal + Bio-gas Area-3: Thermal + Nuclear	TDB, TBD, and GRC

From the above considerations, it is worth combining the benefits of fuzzy type-2, branched controller, AO and AVOA to develop an enhanced LFC strategy for a complex deregulated three-area PS involving nonlinearities of TDB, TBD, and GRC.

1.3 Contributions

In this study, thermal, EV and DRG units are considered in area-1. The DRG of area-1 includes a WTS and an SP system. Area-2 has thermal and gas units, while thermal and geothermal units are connected in area-3. Considering frequency and tie-line power variations of all the three locations, the effects of step load disturbances (SLD) and random load disturbances (RLD) are investigated. The main contributions of this study are:

1. A novel hybrid arithmetic optimized African vulture's optimization algorithm (AOAVOA) is developed.
2. This AOAVOA is used to tune the novel type-2 fuzzy-based proportional-derivative branched with a dual degree-of-freedom proportional-integral-derivative (T2FPD + 2DOFPID) controller.
3. The performance and robustness of the proposed AOAVOA-tuned T2FPD + 2DOFPID controller are thoroughly studied under various practical constraints (plant model perturbation, communication delay, and deregulation) related to the reliable operation of the challenging three-area PS under study.
4. Significant performance improvements in comparison with recently reported control strategies are quantified.

1.4 Objectives

The followings are the objectives of this work:

- To simulate a three-area hybrid PS as stated in the previous subsection.

- To design and simulate the suggested T2FPD + 2DOFPID controller.
- To obtain the optimal settings of the T2FPD + 2DOFPID controller using AOAVOA and other recently reported algorithms (WOA, TLBO, SMA, AO, and AVOA) and compare the dynamic responses in the presence of SLD.
- To obtain the optimal gains of various existing and T2FPD + 2DOFPID controllers using AOAVOA and to compare their dynamic responses in the presence of SLD and RLD.
- To conduct a Bode-based robust stability study.
- To analyze the impact of communication delay, including EV and variable DRG.
- To compare the outcomes of the suggested LFC scheme against some recently reported strategies.

2 System investigated

A complex three-area PS as shown in Fig. 1 with different GENCOs is considered. The system under consideration contains 6 GENCOs with two in each area. In all the three areas, thermal units have reheated turbines, TDB, TBD, and GRC, while Gas plants also have GRC. This makes the power system under investigation more realistic. A GRC of 10% per min and TDB of 0.05% are considered in all thermal generating units. For the gas unit, a GRC of 20% per min is considered in area-2 [4, 16, 44]. Thermal sources contribute 60% of power generation in each area, represented by participation factors ($pf_{11}=pf_{21}=pf_{31}=0.6$), whereas gas contributes 40% of power generation in area-2 and geothermal contributes 40% of power generation in area-3 ($pf_{22}=pf_{32}=0.4$). EV and DRG contribute 10% and 30% of power generation ($pf_{13}=0.1$, $pf_{12}=0.3$) in area-1. The DRG of area-1 includes a WTS and an SP, which are coupled with a steady power input of 0.0005 pu each. The presence of EVs in the system improves its performance by increasing its dynamic behavior. The total load demand of DISCO1 and DISCO2 is set as 0.01 pu. A DPM is used to make agreements between DISCOs and GENCOs. Since there is a controller for each area in the system

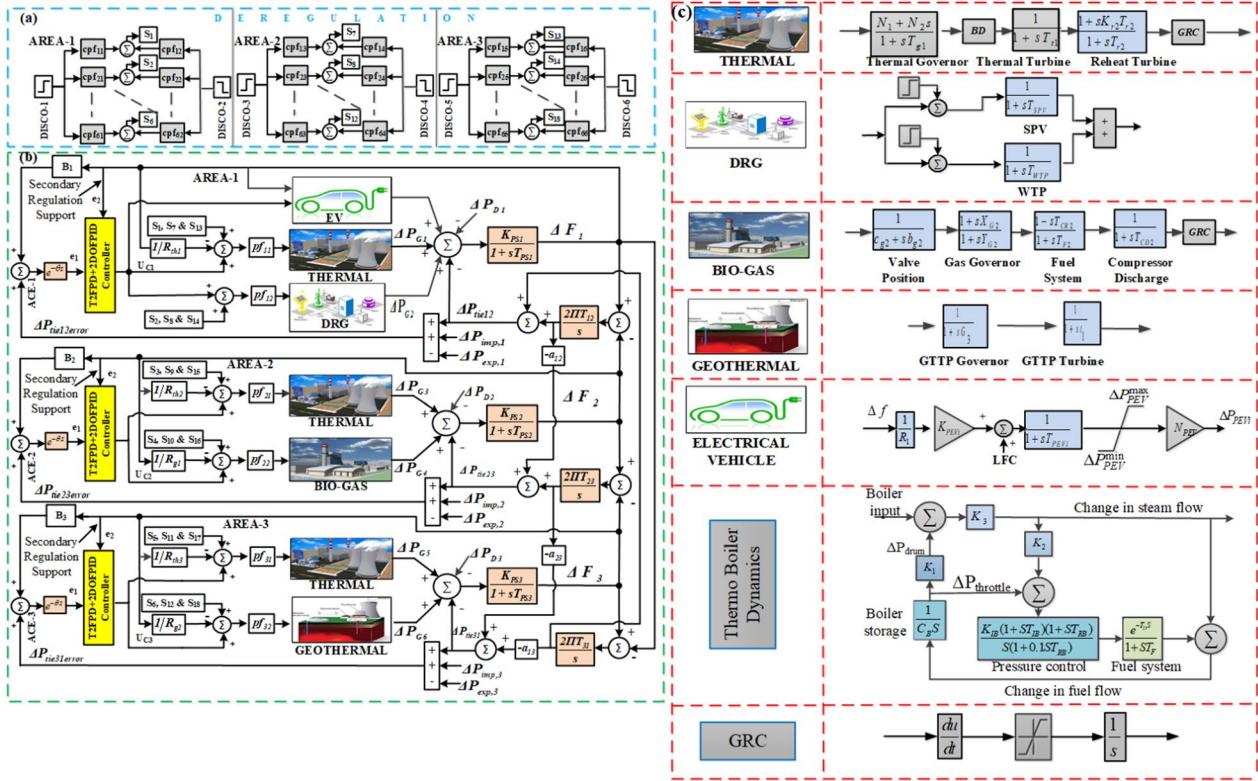


Fig. 1 Schematic of **a** Deregulation **b** Investigated three-area system **c** Models of GENCOs

under consideration, the tie-line power and frequency variances are minimized, and eventually, the area control error (ACE) is also minimized. The combined contribution of cpf_{11} and cpf_{12} is referred to as ' S_1 ', and ' S_2 ' for cpf_{21} and cpf_{22} , etc. S_1 , S_7 , and S_{13} are involved in GENCO-1 (thermal unit of the first area), whereas S_2 , S_8 , and S_{14} are for GENCO-2. A similar trend is followed for the rest of the GENCOs. Elements of the DPM indicate the fraction of power contracted by a DISCO from the associated GENCO. For the studied PS, the DPM [23] is

$$DPM = \begin{bmatrix} cpf_{11} & \cdots & cpf_{16} \\ \vdots & \ddots & \vdots \\ cpf_{61} & \cdots & cpf_{66} \end{bmatrix} \quad (1)$$

The power flowing through the tie-line (scheduled power) is

$$\Delta P_{tiescheduled} = \Delta P_{exp} - \Delta P_{imp} \quad (2)$$

where ΔP_{exp} is the power exported by GENCO in an area from DISCOs of the other two areas [23]. Similarly, ΔP_{imp} is the power imported by GENCO in an area from the rest of the DISCOs. Thus, the error in the tie-line power flow [23] can be expressed by:

$$\Delta P_{tieerror} = \Delta P_{tiescheduled} - \Delta P_{tierated} \quad (3)$$

The area control error (ACE) [55] acts as the input for the controllers which is given as:

$$ACE = \sum B_i \Delta F_i + \Delta P_{tieerror} \quad (4)$$

where B_i is the bias coefficient of the i^{th} area. The notations introduced in this section are appropriately subscripted in Fig. 1 to make them relevant to individual control areas. The GENCO models used in the studied PS are discussed below.

2.1 Thermal unit

The dynamics of a thermal GENCO consist of the following blocks: GRC, TDB, TBD, thermal and reheat turbine. The transfer function models of these blocks are depicted in Fig. 1c, and a brief discussion of the system is presented here.

2.1.1 Generation rate constraint (GRC)

It provides a practical limit to the rate of change in power generation. GRC is always considered as a limiter with the steam turbine as shown in Fig. 1c. It is 10% per min

in this work. The detailed modeling of GRC can be found in [67, 68].

2.1.2 Thermal governor with a dead-band (TDB)

The thermal dead-band is another type of nonlinearity encountered in LFC systems. It is defined as the total magnitude of speed fluctuation in the steady state speed that does not cause the governor valve to change. The TDB is always expressed as a percentage of the rated speed and indicates the level of insensitivity to the speed governing mechanism. Dead-band is depicted by $N_1 + N_2s$, where N_1 and N_2 are the Fourier coefficients. The parameter values of the GDB system are given as $N_1 = 0.8$ and $N_2 = -0.064$ [68, 69].

2.1.3 Thermo-boiler dynamics (TBD)

A boiler is a machine used to generate steam under pressure. The block diagram of a drum-type boiler is shown in Fig. 1c. The transfer functions of the pressure control unit, fuel system and boiler storage are [70]:

$$\left. \begin{aligned} G_{PC}(s) &= \frac{K_{IB}(1+sT_{IB})(1+sT_{RB})}{s(1+0.1T_{RB}s)} \\ G_{FS}(s) &= \frac{e^{-T_D s}}{1+sT_F} \\ G_{BS}(s) &= \frac{1}{sC_B} \end{aligned} \right\} \quad (5)$$

K_1 , K_2 and K_3 are boiler parameters in Fig. 1c. K_{IB} is the boiler integrator gain, T_{IB} is the proportional-integral ratio of the gains, T_{RB} is the recirculation boiler time constant, T_D is the fuel system delay, T_F is the fuel system time constant, and C_B is the boiler storage time constant. The parameter values of the TBD system are given as $K_1 = 0.85$, $K_2 = 0.095$, $K_3 = 0.92$, $C_B = 200$, $T_D = 0$, $T_{IB} = 26$, $K_{IB} = 0.02$, $T_F = 25$ and $T_{RB} = 69$.

2.1.4 Thermal turbine

Two main elements affect the dynamic response: (1) entrained steam between the inlet steam pressure and the turbine's first stage; and (2) the storage action in the reheater that causes the low-pressure stage output to lag behind the high-pressure stage output. Hence, two temporal constants define the turbine transfer function. For simplicity, the turbine is assumed to have a single equivalent time constant as shown in Fig. 1c. The transfer function of the thermal turbine is [68]:

$$G_{RT}(s) = \frac{1}{1+sT_{t1}} \quad (6)$$

where $T_{t1} = 0.3$ is the turbine time constant.

2.1.5 Reheat turbine

Reheaters are specifically designed to raise the saturated steam temperature and give support in regulating steam

exit temperature. The transfer function for the reheat turbine is given by [68]:

$$G_{TT}(s) = \frac{1+sK_{r2}T_{r2}}{1+sT_{r2}} \quad (7)$$

where K_{r2} is the gain of the reheat turbine and T_{r2} is the reheat turbine time constant, and are given as $K_{r2} = 0.3$ and $T_{r2} = 10$ s.

2.2 Geothermal power plant (GTPP) unit

The block diagram of a GTPP is shown in Fig. 1c. The transfer functions of the GTPP governor and GTPP turbine are [71]:

$$\left. \begin{aligned} G_{GTPG}(s) &= \frac{1}{1+sG_3} \\ G_{GTTPT}(s) &= \frac{1}{1+st_3} \end{aligned} \right\} \quad (8)$$

where G_3 and t_3 are the geothermal governor and turbine time constants, respectively, and are given as $G_3 = 0.05$ and $t_3 = 0.1$ [23].

2.3 Bio-gas unit

A bio-gas unit is made up of a valve position, a fuel system, a gas governor, compressor discharge, and GRC. The block diagram of a bio-gas unit is shown in Fig. 1c. The transfer functions of the valve position, fuel system, gas governor, and compressor discharge are [72]:

$$\left. \begin{aligned} G_{VP}(s) &= \frac{1}{c_{g2}+sb_{g2}} \\ G_{GG}(s) &= \frac{1+sX_{G2}}{1+sY_{G2}} \\ G_{FS}(s) &= \frac{1-sT_{CR2}}{1+sT_{F2}} \\ G_{CD}(s) &= \frac{1}{1+sT_{CD2}} \end{aligned} \right\} \quad (9)$$

where c_{g2} and b_{g2} are bio-gas valve operation parameters, while X_{G2} and Y_{G2} are bio-gas governor operation time-constants. T_{CR2} and T_{F2} are bio-gas fuel scheme time constants, and T_{CD2} is the bio-gas compressive discharge time-constant. They are given as $b_{g2} = 0.049$, $c_{g2} = 1$, $X_{G2} = 0.6$, $Y_{G2} = 1.1$, $T_{CR2} = 0.01$, $T_{F2} = 0.239$ s, $T_{CD2} = 0.2$ s, and GRC = 20% per min [23].

2.4 DRG

The solar photovoltaic (SPV) and wind turbine plant (WTP) used in the DRG depicted in Fig. 1c are detailed below.

2.4.1 SPV

The PV system that is connected to the grid is made up of solar panels, converters, power conditioners, and other

connecting equipment. The equivalent PV system transfer function comprising the aforementioned components is [23]:

$$G_{SPV}(s) = \frac{1}{1 + sT_{SPV}} \quad (10)$$

$T_{SPV} = 1.8$ s is the solar PV time constant in this work.

2.4.2 WTP

The transfer function of the WTP system is [23]:

$$G_{WTP}(s) = \frac{1}{1 + sT_{WTP}} \quad (11)$$

where T_{WTP} is the wind turbine time constant which is 1.5 s in this work.

2.5 Electric vehicle (EV)

In this work, an aggregate EV model [73] is considered. The power is directly transferred into the grid during peak hours even if the EV aggregator does not participate in the deregulation. Figure 1c displays the block diagram showing the dynamics of an aggregate EV. To prevent sharp spikes brought about by EVs being disconnected from the grid, dead-band nonlinearity is considered with primary droop settings thereby limiting the bandwidth of operation between ± 20 mHz. K_{PEV} is the EV gain whose value is determined by the state of charge (SOC) of the EV battery and the time constant is denoted by T_{PEV} . K_{PEV} is set to 1 for the idle mode of operation (Fig. 2) while N_{PEV} is the number of EVs in the aggregator. SOC plots are shown in Fig. 2. The parameter values of EV are: $R_{PEV} = 2.399$, $K_{PEV} = 1$, $T_{PEV} = 1$ s, $N_{PEV} = 10,000$ and $\Delta P_{PEV} = \pm 5 \times 10^{-7}$ [23]. ΔP_{PEVi} denotes the incremental power injected in the i^{th} area bounded within ΔP_{PEV}^{\max} and ΔP_{PEV}^{\min} which are [73]:

$$\left. \begin{aligned} \Delta P_{PEV}^{\max} &= + \left[\Delta P_{PEVi} \times \frac{1}{N_{PEV}} \right] \\ \Delta P_{PEV}^{\min} &= - \left[\Delta P_{PEVi} \times \frac{1}{N_{PEV}} \right] \end{aligned} \right\} \quad (12)$$

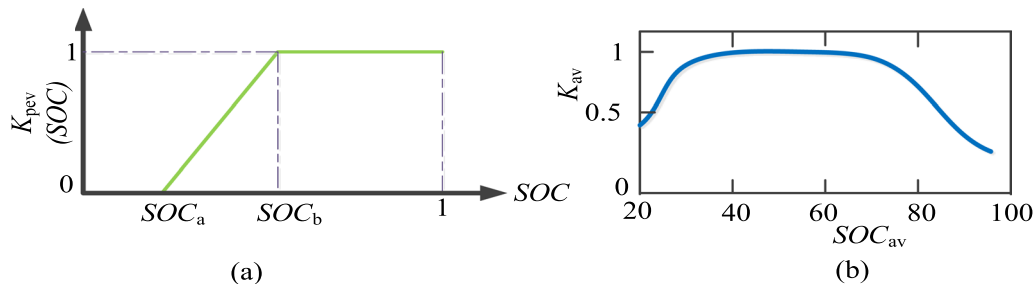


Fig. 2 Characteristic of **a** K_{PEV} vs SOC in idle mode of operation **b** K_{av} vs SOC_{av}

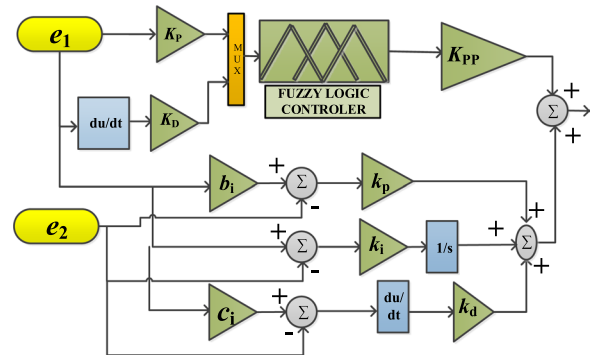


Fig. 3 Block diagram of the T2FPD + 2DOFPID controller

3 Suggested type-2 fuzzy-based control strategy

FLCs are efficient in dealing with nonlinear systems and a variety of operating circumstances [10]. The block diagram of the proposed T2FPD + 2DOFPID controller is given in Fig. 3. As shown, there are two bifurcations (FPD and 2DOFPID) in parallel. The FLC part aids in adjusting to nonlinear dynamics and variations in operative environments subject to the choice of rule-base and membership functions (MFs). A type-2 (T2) fuzzy system (FS) is preferred to avoid the rule-base uncertainties that are present in type-1 (T1) FS [24]. The three-dimensional surface view of the T1FS and T2FS rule-base is given in [28]. A T2FS is described by a 3-D MF [24] as opposed to the 2-D MF of T1FS. It is described in terms of MF $\sigma_{\tilde{A}}(x, \mu)$ subjecting to $x \in X$ and $\mu \in P_x \subseteq [0, 1]$ such that:

$$\tilde{F} = \{((x, \mu), \sigma_{\tilde{F}}(x, \mu)) | \forall x \in X, \forall \mu \in P_x \subseteq [0, 1]\} \quad (13)$$

where $0 \leq \sigma_{\tilde{F}}(x, \mu) \leq 1$. The 3-D MF \tilde{F} can be expressed in the following integral form:

$$\tilde{F} = \int \int_{x \in X, \mu \in P_x} \frac{\sigma_{\tilde{F}}(x, \mu)}{(x, \mu)} P_x \in [0, 1] \quad (14)$$

where the dual integral is used for the T2 set which represents the inclusion of all allowable x and μ . The uncertainties in MF of the T2 fuzzy set \tilde{F} is depicted by a region called the uncertainty footprint (UF), which is the union of all elementary MF lying under $\tilde{F} = 1 \forall \mu \in P_x \subseteq [0, 1]$.

$$Y_{\text{centered}} = \int_{y^1 \in Y^k} \cdots \int_{y^1 \in Y^k} \int_{f^1 \in F^1(x)} \cdots \int_{f^N \in F^N(x)} \left[\sum_{k=1}^N f^k / \sum_{k=1}^N f^k y^k \right] = [u_l, u_r] \quad (18)$$

The complete T2FS mechanism is governed by the operators comprising a fuzzifier, rule-base, inferential system, T-reducer, and defuzzifier [74].

3.1 Fuzzifier

A fuzzifier transforms crisp input sets $[ACE_1, ACE_2 \cdots ACE_n]^T$ into T2 set intervals \tilde{F} .

3.2 Rule-base

Fuzzy rules are constructed keeping in view the convergence nature of the problem. These rules are similar to the type-1 system with the only difference being that MFs are governed. A typical K^{th} rule of T2FLC [74] is given by

$$\text{If } ACE_1 = \tilde{F}_1^k \text{ and } d/dt(ACE) = \tilde{F}_1^k, \text{ then } u = \tilde{G}^k \quad (15)$$

where $k = 1, 2, \dots, N$ and \tilde{G}^k is the corresponding output. N is the maximum number of rules corresponding to the five MFs (5×5).

3.3 Inferential system

The inferential system combines the fuzzy rules to map input T2FS with output T2FS. It evaluates the k^{th} rule to establish the relationship between $f^k(x)$ and $\tilde{f}^k(x)$ as:

$$F^k(x) = [f^k(x), \tilde{f}^k(x)] \quad (16)$$

where

$$f^k(x) = \mu_{-\tilde{r}_1^k}(x_1) \times \mu_{-\tilde{r}_2^k}(x_2) \quad (17a)$$

and

$$\tilde{f}^k(x) = \bar{\mu}_{\tilde{r}_1^k}(x_1) \times \bar{\mu}_{\tilde{r}_2^k}(x_2) \quad (17b)$$

3.4 T-reducer

The T2 set obtained from the inferential system needs to be converted into a T1 set, which is done by the T-reducer. The centered set method of type reducing is [74]:

The Karnik–Mendel method is used to compute the extremities u_l and u_r as [74]:

$$u_l = \sum_{j=1}^N f_l^k y_l^k / \sum_{j=1}^N f_l^k \quad (19a)$$

and

$$u_r = \sum_{j=1}^N f_r^k y_r^k / \sum_{j=1}^N f_r^k \quad (19b)$$

3.5 Defuzzification

The final step of defuzzification reverts crisp output from the type-1 set. Of the several methods of defuzzification, the centroid of the area approach [36] is used which is given by:

$$u_{\text{COA}_r} = \frac{\int_u \mu_A(u) u du}{\int_u \mu_A(u) du} \quad (20)$$

The orientation of various T1 and T2 MFs are given in Fig. 4. The triangular and trapezoidal MFs (rightmost in the upper row of Fig. 4) in [75] for T1FS are modified as presented in the lower rightmost portion of Fig. 4. In this MF, the five linguistic variables are high-negative (rf_{n2}), little-negative (rf_{n1}), zero (rf_{z0}), little-positive (rf_{p1}), and high-positive (rf_{p2}). This MF is considered because of its ease of use and rapid computational speed. For this study, the range of MF is chosen from -1 to 1 [76], and the scaling factors for the input and output are adopted from [25]. The fuzzy rule-base for the proposed controller (Table 2) is adopted from [6]. Reference [55] has demonstrated the merits of a branched controller, while such controller can be further enhanced by adding extra DOF in the branched path. The dual-DOF results in the reduction

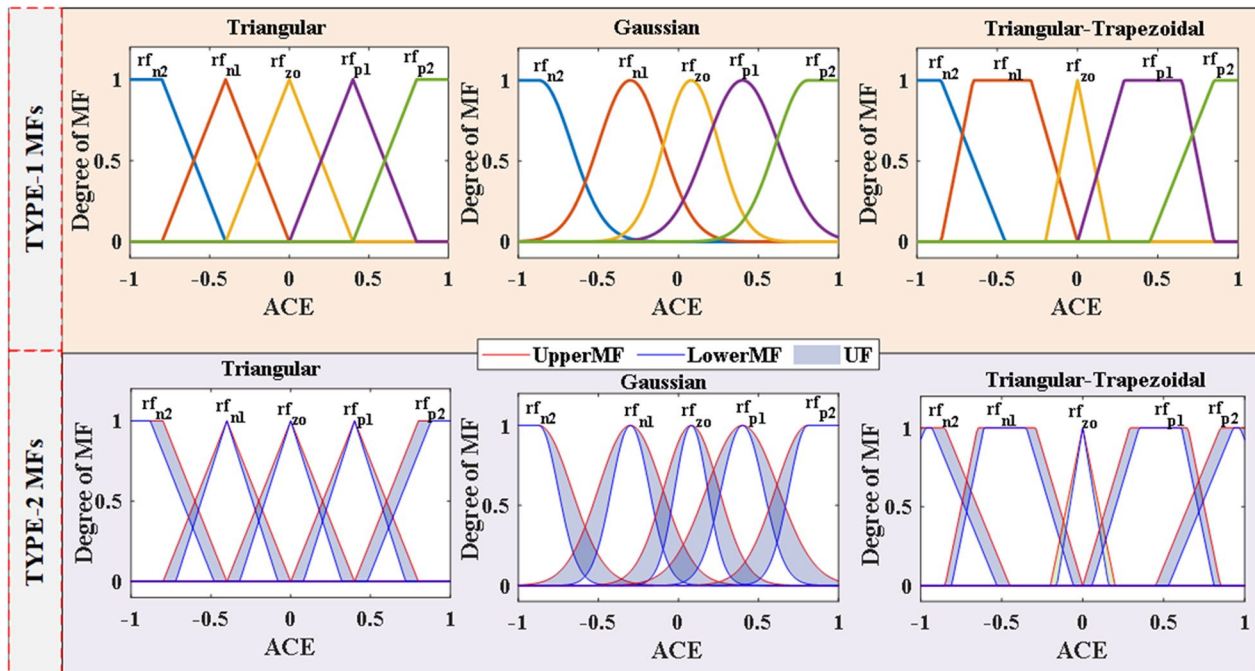


Fig. 4 Various type-1/type-2 MFs

Table 2 Rule-base of the FLC (for T1FS and T2FS)

ACE	ΔACE				
	rf_{n2}	rf_{n1}	rf_{zo}	rf_{p1}	rf_{p2}
rf_{n2}	rf_{n2}	rf_{n2}	rf_{n1}	rf_{n1}	rf_{zo}
rf_{n1}	rf_{n2}	rf_{n1}	rf_{n1}	rf_{zo}	rf_{p1}
rf_{zo}	rf_{n1}	rf_{n1}	rf_{zo}	rf_{p1}	rf_{p1}
rf_{p1}	rf_{n1}	rf_{zo}	rf_{p1}	rf_{p1}	rf_{p2}
rf_{p2}	rf_{zo}	rf_{p1}	rf_{p1}	rf_{p1}	rf_{p2}

of overshoot, settling time, and rejection of noise, and it comprises two input signals (reference signal and measured output with frequency fluctuations).

4 Optimization

4.1 Arithmetic optimizer

AO is a class of population-generated metaheuristic (PGM) approach [77]. The majority of PGM approaches initialize with a set of random solutions, which are incrementally improved through repetitive iterations and evaluated regularly by a given cost function. As PGM approaches are uncertain, solving in a solitary run is rare. As a result, having a large number of repeats increases the likelihood of getting a global optimum. AO starts with some candidate solutions (X) generated randomly in each iteration [78], shown as:

$$X = \begin{pmatrix} x_{1,1} & \dots & x_{1,n} \\ \vdots & \ddots & \vdots \\ x_{N,1} & \dots & x_{N,n} \end{pmatrix} \quad (21)$$

From (21), the best/fineest solution is determined. Once X is initialized, the optimizer decides the optimization phase to enter using the math optimizer acceleration (MOA) function computed as [77]:

$$MOA(C_{Iter}) = Min + C_{Iter} \times \left(\frac{Max - Min}{M_{Iter}} \right) \quad (22)$$

The above equation gives the function value $MOA(C_{Iter})$ at the i th iteration. M_{Iter} denotes the maximum iteration count, while Min/Max represent the minimum/maximum MOA values, respectively. The exploration and exploitation phases are elaborated below.

4.1.1 Exploration phase

The math optimization probability (MOP) is expressed by [77]:

$$MOP(C_{Iter}) = 1 - \frac{C_{Iter}^{\frac{1}{\alpha}}}{M_{Iter}^{\frac{1}{\alpha}}} \quad (23)$$

where $MOP(C_{Iter})$ is the value of MOP in the current iteration (C_{Iter}). $\alpha=5$ (in this work) is responsible for the exploitation accuracy. Depending on whether MOA

is greater than r_1 or not, AO enters the exploration or exploitation phase. This determines the phase that AO must enter. Exploration is carried out by MOP and other functions and thereby the candidate solutions are updated using these operators in this phase. The following rule [77] is used to repeat the behavior of arithmetic operators by updating the positions:

$$x_{i,j}(C_{\text{Iter}} + 1) = \begin{cases} \text{best}(x_j) \div (MOP + \varepsilon) \times ((UB_j - LB_j) \times \mu + LB_j); & r_2 < 0.5 \\ \text{best}(x_j) \times MOP \times ((UB_j - LB_j) \times \mu + LB_j); & \text{Otherwise} \end{cases} \quad (24)$$

where the i th solution in the next iteration is specified by $x_i(C_{\text{Iter}} + 1)$. The j th position of the i th solution in the existing iteration is $x_i(C_{\text{Iter}})$, and the best (x_j) is the

is executed thereby ignoring the division. μ enhances the diversity of both operator values and the search space, and hence it is ensured that AO is not stuck at any local optima.

4.1.2 Exploitation phase

When $r_1 > MOA$, the exploitation phase is initialized. In this phase, either the 'addition' or the 'subtraction' operator is executed as per Fig. 5. The candidate solutions are updated as follows [77]:

$$x_{i,j}(C_{\text{Iter}} + 1) = \begin{cases} \text{best}(x_j) - (MOP + \varepsilon) \times ((UB_j - LB_j) \times \mu + LB_j); & r_3 < 0.5 \\ \text{best}(x_j) + MOP \times ((UB_j - LB_j) \times \mu + LB_j); & \text{Otherwise} \end{cases} \quad (25)$$

j th position in the best-obtained solution until then. ε takes an integer value, and UB_j/LB_j represent the upper/lower j th positions, respectively. $\mu=0.5$ (in this work) is a parameter that controls the search process. If $r_1 < MOA$, the exploration phase begins as per (24). A second beta-distributed random number (r_2) is generated. If $r_2 < 0.5$, the division operator is executed thereby ignoring the multiplication operator, whereas if $r_2 \geq 0.5$, multiplication

Unlike both operators of (24), Eq. (25) will be able to converge at the optimal solution. Another random number (r_3) is generated. If $r_3 < 0.5$, the '-' operator is executed, while on the other hand, the '+' operator will be at work when $r_3 \geq 0.5$. When the '-' operator is at work, the '+' operator is ignored and vice versa. The scaling coefficient (μ) plays the same role as in the exploration phase to enhance the diversity of the search space. This helps

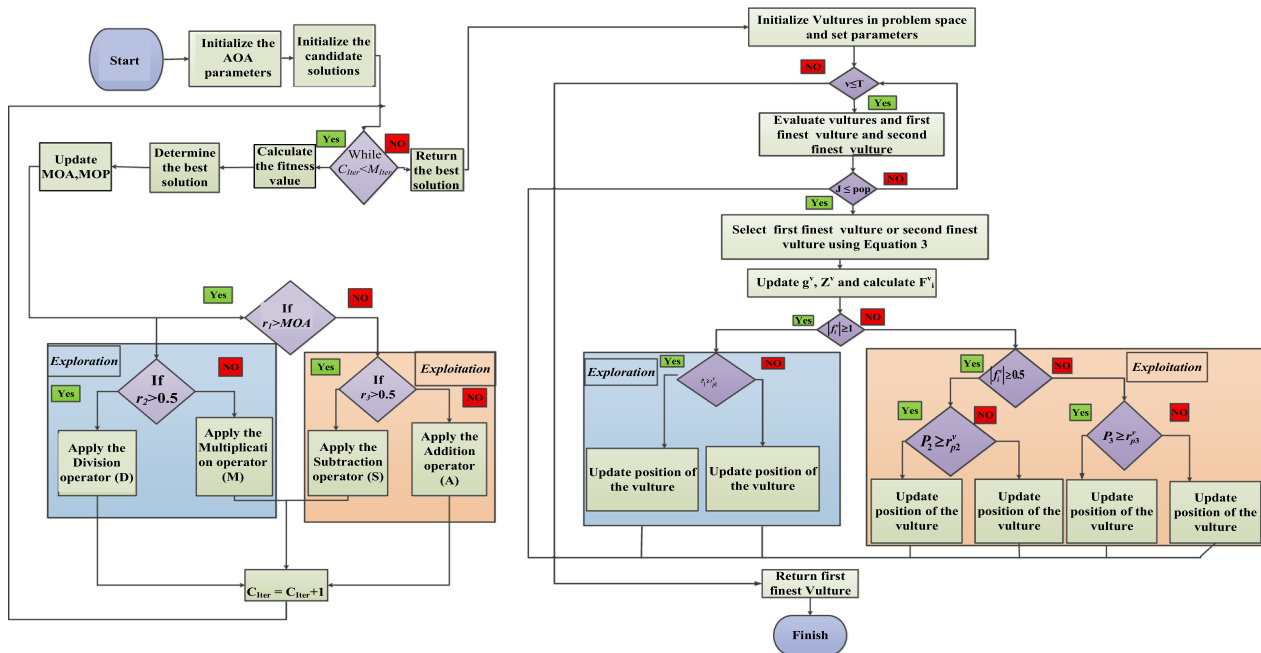


Fig. 5 Flow chart of hybrid AOA/VOA

AO to avoid getting stuck in local optima. The candidate solutions are further updated using (25).

4.2 African vulture's optimizer

The AVOA algorithm was first reported in [64], and mimics the foraging behavior and dwelling behavior of Africa's vultures. The African vulture population consists of ' N ' vultures and the algorithm user determines the size of ' N ' based on the requirement. Each vulture has a D -dimensional position space, and the size of D is determined by the problem's dimension. Similarly, depending on the difficulty of the task, T is the maximum iterations/vulture actions. Therefore, each vulture's position i ($1 \leq i \leq N$) at a particular iteration v ($1 \leq v \leq T$) can be expressed with the following position vector [79]:

$$Y_i^v = [y_{i1}^v, \dots, y_{id}^v, \dots, y_{iD}^v] \quad (26)$$

The African vulture population is divided into three groups based on their living patterns. If the vulture's superior position is measured using the fitness value (of the likely solution), the first flock is tasked with locating the finest possible position among all vultures, while the subsequent flock believes the aforementioned likely solution to be the best among all the vulture positions. In the foraging stage, AVOA can be separated into the following five steps to simulate different vulture behaviors.

4.2.1 Step-1 (Population bunch)

The vulture representing the finest answer is positioned in the first group while the vulture representing the second-finest position is placed in the second group. The remaining vultures are classified as the third group.

4.2.2 Step-2 (Hunger of vultures)

If the vulture is not starving, it has sufficient strength to travel great distances in quest of food. Alternatively, if the vulture is extremely famished, it lacks the physical strength to sustain a long-distance journey. As a result, hungry vultures will become more rampant, and instead of seeking food on their own, they will stick close to the vultures that have food. The exploration and exploitation stages of vultures can thus be formed based on the above behavior. The degree of hunger indicates when vultures are transitioning from the stage of exploration to exploitation.

4.2.3 Step-3 (Exploration stage)

With their exceptional vision, vultures possess the ability to find their prey quickly. Therefore, when searching for food, vultures spend more time probing their surroundings and fly long distances in search of prey. In AVOA, vultures can examine a variety of random regions using

two separate strategies, while the parameter P_1 decides the selection of any one of the strategies.

4.2.4 Step-4 (Exploitation stage)

If $|f_i^v|$ has a value between 0.5 and 1, the vulture will reach the intermediate stage. In this stage, P_2 is the variable which is in the range [0,1], and determines whether the vulture competes for food or flies in a circular pattern. Hence, when reaching this stage, $rand_{p2}^v$ is a random number in the range [0,1], which is generated before the vulture acts. When $rand_{p2}^v \leq P_2$ the vultures perform a food contest, whereas when $rand_{p2}^v > P_2$, the revolving flight action is carried out. When $|f_i^v| \geq 0.5$ the vulture is filled with food and energized. Hence, while the vultures are all together at the same moment, the strong vultures will not share their food. To gather food, the feeble ones try to form a swarm and attack the stronger ones. When the vulture is energized, it will not only demonstrate prey contest behavior but also fly at a high altitude. This behavior is modeled by AVOA using a helical model.

4.2.5 Step-5 (Exploitation stage)

When $|f_i^v| < 0.5$, almost the whole population of vultures is fed. However, the best two kinds of vultures have gone starving and feeble after a lengthy period of hunting. The prey will be targeted such that different vultures will concentrate on an identical source of prey. Hence, in this stage, there is a variable P_3 in the range [0,1] that determines aggressive behavior. Before entering this stage, a random number $rand_{p3}^v$ in the range [0,1] is generated. When $rand_{p3}^v \leq P_3$, the vultures exhibit aggressive behaviour, and when $rand_{p3}^v > P_3$, they exhibit attack behavior. More mathematical details about the aforementioned AVOA steps are presented in [28].

4.3 Proposed AOAVOA

The motivation for developing a hybrid AOAVOA by combining the merits of AO and AVOA is drawn from [66, 80]. Reference [66] hybridizes GWO and CSA whereas HHO and ICA are hybridized in [80]. Both AO and AVOA have their respective strengths and weaknesses. AO shows better convergence than other contemporary algorithms such as PSO, EO, HHO, SMA, TLBO and WOA, as demonstrated in [24]. On the other hand, AVOA also shows better convergence than some contemporary algorithms such as PSO, SMA, AO, and TLBO, as given in [28]. However, AO has some drawbacks, e.g., its location update based on the ideal value, premature convergence, and low solution precision put AO at risk of entering a local optimum [81]. Similarly, AVOA also has some disadvantages such as the existence of poor exploration–exploitation tradeoff and quickly reaching a local optimum [79]. In this study, it

aims to achieve an effective optimal solution (parameters of the suggested controller using the hybrid AOAVOA by combining the merits of AO and AVOA). As seen in the flow chart described in Fig. 5, AOAVOA consists of two main phases (AO and AVOA) in cascade. The steps of the AO algorithm [24] are executed initially, and the best solution of AO is then given for initializing vultures in AVOA. Finally, the steps of the AVOA algorithm [28] are executed. Integration of time-weighted absolute error (ITAE) given in (25) is chosen as the cost function and the justification for the same can be found in the subsequent section. For $0.001 \leq K_i \leq 2$, the population-size and iteration-count are set to 5 and 20, respectively. The goal of employing AOAVOA for this study is to find the optimal controller parameters such that the following objective function (OF) [28] is minimized:

$$J_{ITAE} = \int_0^{T_{sim}} \{|\Delta F_1| + |\Delta F_2| + |\Delta F_3| + |\Delta P_{tie12}| + |\Delta P_{tie23}| + |\Delta P_{tie31}|\} t dt \quad (27)$$

where ΔF_1 ; ΔF_2 ; ΔF_3 and ΔP_{tie12} ; ΔP_{tie23} ; ΔP_{tie31} are the frequency fluctuations in areas-1, 2 and 3 and tie-line power fluctuations connecting areas-1&2, areas-2&3 and areas-3&1, respectively. T_{sim} is the simulation time.

5 Results and analysis

The performance of the AOAVOA-tuned T2FPD+2DOF-PID control strategy is demonstrated by simulating the interconnected system elucidated in Fig. 1. Nonlinearities (in GRCs of GENCOs) shown in Table 3 are considered to investigate the system's realistic operation. The DISCO's load demand is chosen as 0.01 pu whereas the DPM used in this study is adopted from [28]. The dynamic responses resulting from controllers designed using various MFs discussed in Fig. 4 (subjected to SLD) are compared in Fig. 6a. The type-2 customized triangular-trapezoidal MF used in this work produces better performance than the triangular and Gaussian membership functions. In this section, the supremacy of AOAVOA-tuned T2FPD+2DOFPID control strategy over other

controllers and optimizers is established under poolco, bilateral transaction, and contract violation scenarios.

5.1 Poolco-based scheme

In this case, only one customer is considered. This is a government entity that grants power to everyone. Poolco is responsible for maintaining the system and connecting the buyer and vendor by selecting the bidder with the lowest price. A region's GENCOs and DISCOs (with equitable GENCOs) are eligible for LFC participation. Each GENCO is now able to take part in LFC using the following participation factors: $pf_{11} = 0.1$, $pf_{12} = 0.3$, $pf_{13} = 0.6$, $pf_{21} = 0.6$, $pf_{22} = 0.4$, $pf_{31} = 0.6$, and $pf_{32} = 0.4$. The load change is considered only in area-1 (areas-2 and 3 are unchanged). It is assumed that the load is demanded only by DISCOs from its own area GENCOs. The load

demand of all DISCOs is assumed to be 0.005 ($P_{L1} = P_{L2} = P_{L3} = P_{L4} = P_{L5} = P_{L6} = 0.005$ pu). The DISCO's load demand is chosen as 0.01 pu whereas the DPM used in this study is adopted from [28]. For this case, the equations for $P_{tiescheduled}$ and power generation in steady state are adopted from [82]. GENCOs generate steady-state power ($\Delta P_{G1} = 0.0055$, $\Delta P_{G2} = 0.0065$, $\Delta P_{G3} = 0.0030$, $\Delta P_{G4} = \Delta P_{G5} = \Delta P_{G6} = 0$, $\Delta P_{tie12scheduled} = 0.0020$, $\Delta P_{tie23scheduled} = \Delta P_{tie31scheduled} = 0$). The GENCO outputs are presented in Fig. 6b whereas the actual tie-line power deviations are shown in Fig. 6c. In steady state, all generations reach their specified values (Fig. 6b). Since no power is required by area-2 and 3, tie-line power flow in the steady state is set to zero (Fig. 6c).

5.1.1 Performance of suggested AOAVOA

To compare the effectiveness of AOAVOA with other algorithms (WOA, EO, SMA, AO, AVOA) in tuning the T2FPD+2DOFPID controller, a population-size of 5 and an iteration-count of 20 are chosen for $0.01 \leq K_i \leq 2$ with minimizing ITAE as the cost function. As shown in

Table 3 GENCOs' involvement and GRC [23]

AREA-1				AREA-2				AREA-3			
GENCOs	Participation	GRCs		GENCOs	Participation	GRC		GENCOs	Participation	GR	
		UB	LB			UB	LB			UB	LB
Thermal	60%	10%	−10%	Thermal	60%	10%	−10%	Thermal	60%	10%	−10%
DRG	30%	−	−	Gas	40%	20%	−20%	GTPP	40%	−	−
EV	10%	−	−								

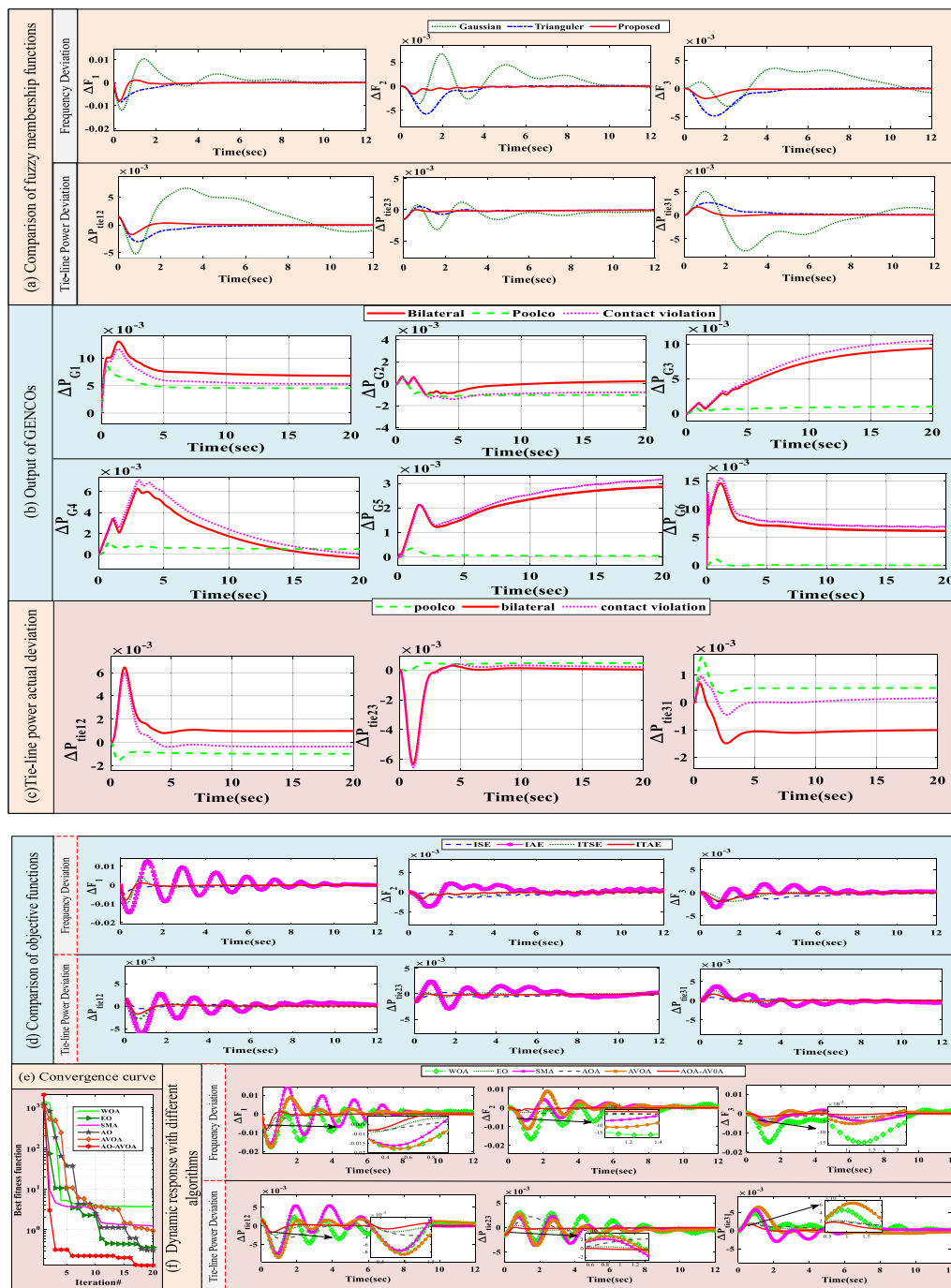


Fig. 6 Comparing MFs, the output of GENCOs, tie line actual derivations, FODs, and dynamic responses of optimizers for Poolco scenario

Fig. 6d, choosing ITAE as the cost function results in better dynamic responses than IAE, ISE, and ITAE.

Hence, ITAE is used as OF in this work. The convergence characteristics of different algorithms are represented by their respective figure of demerits (FODs) in Fig. 6e. It is proved that AOA-VOA converges more

quickly and has a higher fitness value than other algorithms at the end of 20 iterations. Table 4 displays the T2FPD+2DOFPID controller settings produced using various optimization strategies. It is evident from Table 4 and the responses to 1% SLD shown in Fig. 6f that the ITAE value of the dynamic response is better

Table 4 Settings of proposed T2FPD + 2DOFPID controller obtained from different optimizers

Optimization	Gains	Area-1	Area-2	Area-3	ITAE	Optimization	Gains	Area-1	Area-2	Area-3	ITAE
AOAVOA	K_P	2	0.3864	0.0645	0.1266	SMA	K_P	0.5921	0.2472	0.0100	0.6203
	K_D	0.0364	0.0646	0.0018			K_D	0.0167	0.0188	0.0102	
	K_{PP}	1.9690	0.0020	0.0020			K_{PP}	0.3777	0.0209	0.8207	
	b_i	0.0642	0.0160	0.0022			b_i	0.5146	0.0100	0.0101	
	c_i	0.2772	0.0239	0.0021			c_i	0.0378	0.0105	0.0102	
	k_p	2	1.9371	0.3759			k_p	0.1902	0.0112	0.0105	
	k_d	1.7993	1.2320	0.7875			k_d	0.1070	0.7392	1.4544	
AO	k_j	0.1444	0.5853	0.0019	0.1775	EO	k_j	0.7531	0.0104	0.0166	0.1458
	K_P	2	0.0756	1.4570			K_P	0.2354	0.2144	0.1516	
	K_D	0.0144	1.9874	0.0507			K_D	0.3526	0.2999	0.0359	
	K_{PP}	0.8801	0.2332	0.0660			K_{PP}	0.8645	0.1399	0.1261	
	b_i	0.001	0.001	1.9894			b_i	1.7296	0.0012	0.0820	
	c_i	0.3585	0.0581	1.9690			c_i	1.5641	0.4245	0.1488	
	k_p	1.8749	0.8801	0.0756			k_p	1.6093	0.1863	0.5261	
AVOA	k_d	1.9621	0.5051	0.0136	0.6677	WOA	k_d	0.7087	0.5037	0.3240	1.8974
	k_j	0.0548	0.1248	0.001			k_j	0.0643	0.2264	0.0013	
	K_P	0.0016	0.0664	0.0562			K_P	0.0022	0.0022	0.0022	
	K_D	0.0015	0.0373	0.2374			K_D	0.0022	0.0022	1.6072	
	K_{PP}	0.0920	0.0953	0.0039			K_{PP}	0.0022	0.0022	0.0025	
	b_i	0.0812	0.1045	0.0752			b_i	0.0022	0.0022	0.0022	
	c_i	0.0752	0.3011	0.7056			c_i	1.6076	0.0022	0.0057	
	k_p	0.0469	0.2978	1.6729			k_p	0.1038	0.0022	0.0022	
	k_d	0.0015	0.1504	0.0020			k_d	0.0022	0.0057	0.0022	
	k_j	0.0201	0.0015	0.0379			k_j	0.0022	0.0057	0.0057	

Table 5 Quantitative performance comparison of different optimizers

Optimization	Signal deviation	T_s (s)	MOS	MUS	Optimization	Signal deviation	T_s (s)	MOS	MUS
AOAVOA	ΔF_1 (Hz)	4.2093	0.0011	- 0.0080	SMA	ΔF_1 (Hz)	29.8430	0.0148	- 0.0162
	ΔF_2 (Hz)	22.5840	1.4460×10^{-5}	- 0.0016		ΔF_2 (Hz)	14.0437	0.0045	- 0.0069
	ΔF_3 (Hz)	9.3579	$- 9.3254 \times 10^{-6}$	- 0.0018		ΔF_3 (Hz)	14.2628	0.0018	- 0.0047
	ΔP_{tie12} (p.u)	6.6922	3.4817×10^{-4}	- 0.0017		ΔP_{tie12} (p.u)	16.3211	0.0055	- 0.0076
	ΔP_{tie23} (p.u)	26.3147	6.8055×10^{-6}	- 0.0015		ΔP_{tie23} (p.u)	14.5814	0.0023	- 0.0037
	ΔP_{tie31} (p.u)	22.9936	0.0017	- 0.0017		ΔP_{tie31} (p.u)	16.2408	0.0057	- 0.0057
AOA	ΔF_1 (Hz)	5.3930	3.2938×10^{-5}	- 0.0083	EO	ΔF_1 (Hz)	4.5519	2.6826×10^{-5}	- 0.0088
	ΔF_2 (Hz)	6.3982	9.2332×10^{-5}	- 0.0031		ΔF_2 (Hz)	5.5820	2.7634×10^{-5}	- 0.0026
	ΔF_3 (Hz)	5.7372	5.8576×10^{-6}	- 0.0035		ΔF_3 (Hz)	8.4242	2.7519×10^{-5}	- 0.0028
	ΔP_{tie12} (p.u)	13.0987	4.2483×10^{-5}	- 0.0035		ΔP_{tie12} (p.u)	6.1347	1.2026×10^{-4}	- 0.0025
	ΔP_{tie23} (p.u)	12.4469	0.0022	- 0.0022		ΔP_{tie23} (p.u)	12.4566	4.0268×10^{-4}	- 0.0015
	ΔP_{tie31} (p.u)	21.2614	0.0019	- 0.0019		ΔP_{tie31} (p.u)	11.3618	0.0021	- 0.0021
AVOA	ΔF_1 (Hz)	27.9726	0.0084	- 0.0178	WOA	ΔF_1 (Hz)	24.0893	0.0035	- 0.0177
	ΔF_2 (Hz)	29.2780	0.0089	- 0.0114		ΔF_2 (Hz)	26.3178	0.0017	- 0.0167
	ΔF_3 (Hz)	28.0849	0.0014	- 0.0060		ΔF_3 (Hz)	26.6302	0.0018	- 0.0149
	ΔP_{tie12} (p.u)	28.0390	0.0018	- 0.0085		ΔP_{tie12} (p.u)	26.0189	0.0023	- 0.0078
	ΔP_{tie23} (p.u)	28.6011	0.0028	- 0.0037		ΔP_{tie23} (p.u)	29.3793	0.0030	- 0.0030
	ΔP_{tie31} (p.u)	28.3014	2.1851×10^{-4}	- 0.0063		ΔP_{tie31} (p.u)	20.6946	0.0013	- 0.0047

Table 6 Settings of different controllers obtained from AOAVOA

Controller	Gains	Area-1	Area-2	Area-3	ITAE	Controller	Gains	Area-1	Area-2	Area-3	ITAE
T2FPD + 2DOFPID	K_P	2	0.3864	0.0645	0.1266	T1FPD + 2DOFPID	K_P	0.2050	0.000546	1.8691	3.2637
	K_D	0.0364	0.0646	0.0018			K_D	0.1748	0.0424	1.9124	
	K_{PP}	1.9690	0.0020	0.0020			K_{PP}	0.0990	2	0.0567	
	b_i	0.0642	0.0160	0.0022			b_i	0.0597	0.0418	0.4324	
	c_i	0.2772	0.0239	0.0021			c_i	2	1.2885	0.0442	
	k_p	2	1.9371	0.3759			k_p	0.0519	0.0211	0.0049	
	k_d	1.7993	1.2320	0.7875			k_d	0.0602	0.2548	2	
	k_i	0.1444	0.5853	0.0019			k_i	0.3241	0.0417	0.000771	
T1FID + 2DOFPID	K_P	0.1385	2	0.0533	0.6864	T2FID + PD	K_P	0.3140	0.0284	0.0650	0.6501
	K_D	0.0656	0.6238	0.1643			K_d	1.9792	0.1325	1.6262	
	K_I	2	0.0012	0.0011			K_i	0.5103	2	0.0273	
	b_i	0.5205	0.0012	0.1039			K_{pp}	0.2577	0.0293	0.0650	
	c_i	0.2214	0.0012	0.0901		K_{dd}	2	0.0991	2	0.2976	
	k_p	2	1.2261	0.1688		T1FID + PD	K_P	1.8233	1.9772		0.0024
	k_d	0.1788	0.1373	0.0981			K_d	0.0554	0.3016		0.3363
	k_i	0.0531	0.1433	0.0012			K_i	1.8920	0.0012		0.1531
PID	K_P	0.0001	0.2328	0.0001	0.7624		K_{pp}	2	0.0839	0.0336	
	K_I	0.0001	0.1297	0.0001		K_{dd}	1.9100	1.9792	0.0012		
	K_D	0.0001	0.0887	0.0118							

for AOAVOA. The comparison of time-domain matrices including settling-time (T_s), maximum overshoot (MOS), and maximum undershoot (MUS) for various algorithms is presented in Table 5 to further vindicate the effectiveness of AOAVOA.

5.1.2 Performance of T2FPD + 2DOFPID controller optimized by AOAVOA

The suggested AOAVOA is used to find the optimal settings of controllers such as T2FPD + 2DOFPID, type-1 fuzzy PD branched with 2-DOFPID (T1FPD + 2DOFPID), type-2 fuzzy integral-derivative branched with 2DOF PID (T2FID + 2DOFPID), type-2 fuzzy ID + PD (T2FID + PD), type-1 fuzzy ID + PD (T1FID + PD) and PID. The AOAVOA-based settings of various configurations are listed in Table 6. As is evident from Table 6, the suggested T2FPD + 2DOFPID controller results in dynamic responses with the smallest ITAE value. To explore the disturbance-rejection capabilities of the system, an SLD of 1% (0.01 pu) is applied to all areas. The responses of different controllers are shown in Fig. 7a. It is clear that the AOAVOA-tuned T2FPD + 2DOFPID controller shows better dynamic performance than the other configurations. The AOAVOA-tuned T2FPD + 2DOFPID controller considerably reduces the undershoots, overshoots, and settling time as seen in Table 7. Figure 7b illustrates the comparison of the control efforts. In a practical PS, RLD is inevitable. Hence, with the help of RLD applied in area-1, the dynamic

responses of different controllers are compared in Fig. 7c. The AOAVOA-based controller gains in the presence of this RLD pattern are shown in Table 8. From Fig. 7c, it is evident that the suggested controller restores normalcy more quickly and smoothly than other controller configurations. It is worth mentioning that system stability is maintained even under random loads. Table 9 describes the statistics of 5 independent runs with different algorithms, comprising the maximum ($ITAE_{MAX}$), minimum ($ITAE_{MIN}$), average ($ITAE_{AVG}$) and standard deviations ($ITAE_{STD}$) of ITAE values obtained from the five independent runs. From Table 9, the superiority of the proposed AOAVOA over the EO, AO, and AVOA algorithms is further affirmed.

5.1.3 Case studies

5.1.3.1 Impact of DRG on system performance DRG units contribute to controlling power output and frequency deviation. To assess the effects of DRG units on system performance, the DRG in area-1 is operated in constant and variable input modes to investigate its impact on dynamic responses. For DRG analysis, the following step-change pattern is considered:

$$x(t) = [u(t) + u(t - 10) + u(t - 20) - 2u(t - 30)] \times 10^{-3} \quad (28)$$

where $u(t)$ is the unit step signal. The AOAVOA-tuned T2FPD + 2DOFPID settings with constant DRG are given

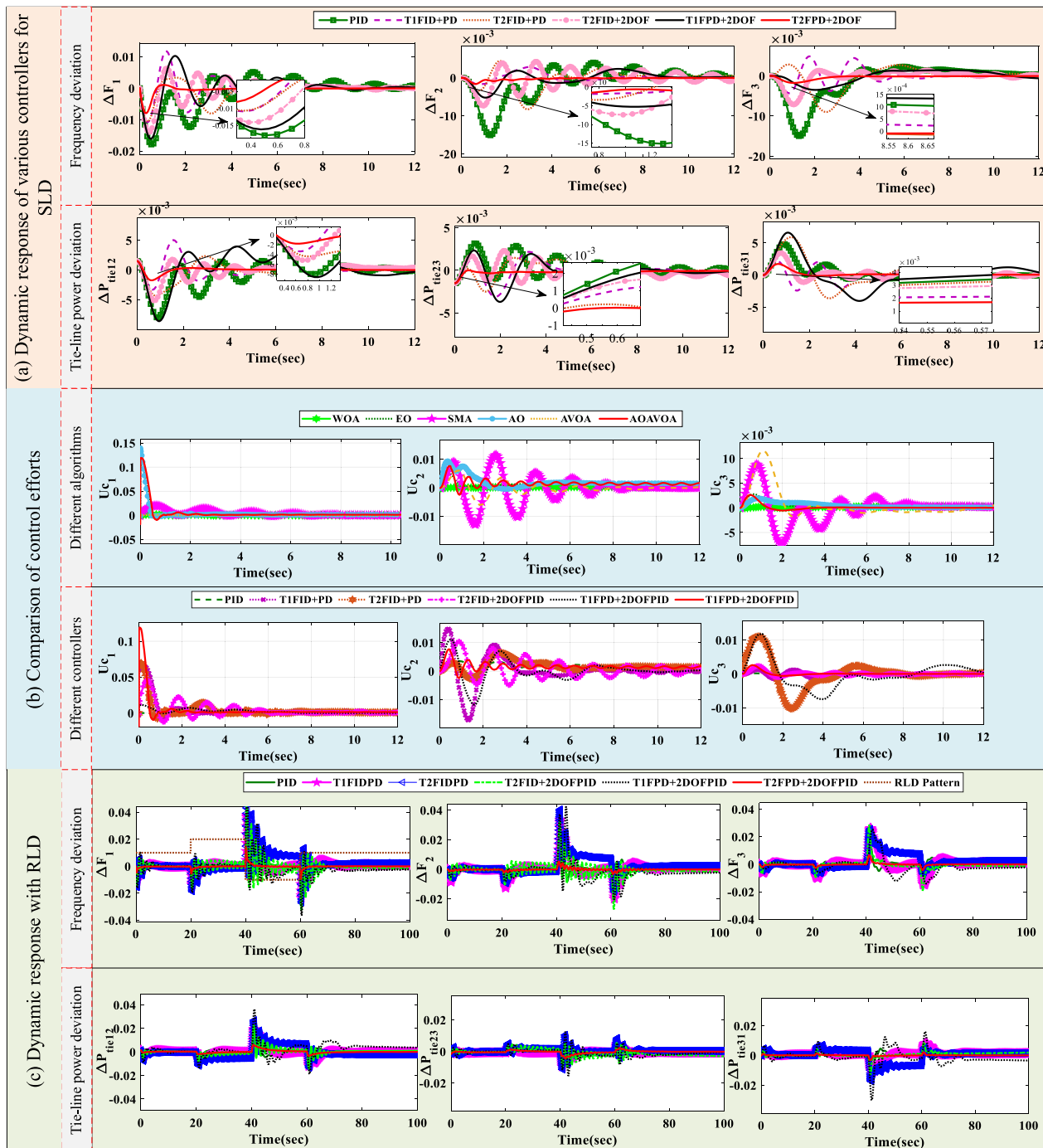


Fig. 7 Dynamic response with SLD, RLD and required control efforts

in Table 4. The plots for variations in the dynamics of renewable energy sources (using the settings in Table 4) are shown in Fig. 8a. From Fig. 8a, it is clear that frequency fluctuations are mitigated and system stability is maintained even in the presence of variable DRG.

5.1.3.2 Impact of communication delay Communication time delays (CTDs) of $\theta = 50$ ms and $\theta = 100$ ms are applied to the controller output. The resulting responses are compared with that of a delay-free system as shown in Fig. 8b. As seen, the ability of the suggested strategy to

Table 7 Quantitative performance comparison of different controllers

Controller	Signal deviation	T_s (s)	MOS	MUS	Controller	Signal deviation	T_s (s)	MOS	MUS
T2FPD + 2DOFPID	ΔF_1 (Hz)	4.2093	0.0011	-0.0080	T2FID + PD	ΔF_1 (Hz)	13.9449	0.0034	-0.0106
	ΔF_2 (Hz)	22.5840	1.4460×10^{-5}	-0.0016		ΔF_2 (Hz)	14.8205	0.0044	-0.0083
	ΔF_3 (Hz)	9.3579	-9.3254×10^{-6}	-0.0018		ΔF_3 (Hz)	14.4317	0.0028	-0.0090
	ΔP_{tie12} (p.u)	6.6922	3.4817×10^{-4}	-0.0017		ΔP_{tie12} (p.u)	17.7959	0.0024	-0.0043
	ΔP_{tie23} (p.u)	26.3147	6.8055×10^{-6}	-0.0015		ΔP_{tie23} (p.u)	27.5125	0.0015	-0.0025
	ΔP_{tie31} (p.u)	22.9936	0.0017	-0.0017		ΔP_{tie31} (p.u)	21.4180	8.2676×10^{-4}	-0.0059
T1FPD + 2DOFPID	ΔF_1 (Hz)	29.2357	0.0103	-0.0161	T1FID + PD	ΔF_1 (Hz)	29.6985	0.0118	-0.0118
	ΔF_2 (Hz)	21.7324	0.0024	-0.0052		ΔF_2 (Hz)	27.8472	0.0029	-0.0029
	ΔF_3 (Hz)	28.8475	0.0014	-0.0035		ΔF_3 (Hz)	28.5993	0.0049	-0.0049
	ΔP_{tie12} (p.u)	27.1038	0.0040	-0.0086		ΔP_{tie12} (p.u)	29.8058	0.0050	-0.0050
	ΔP_{tie23} (p.u)	28.4228	0.0023	-0.0037		ΔP_{tie23} (p.u)	29.7735	0.0022	-0.0031
	ΔP_{tie31} (p.u)	27.7496	0.0012	-0.0066		ΔP_{tie31} (p.u)	29.8012	0.0022	-0.0024
T2FID + 2DOFPID	ΔF_1 (Hz)	26.5585	0.0063	-0.0140	PID	ΔF_1 (Hz)	13.9831	0.0052	-0.0179
	ΔF_2 (Hz)	29.8186	0.0043	-0.0074		ΔF_2 (Hz)	14.9718	0.0040	-0.0151
	ΔF_3 (Hz)	27.7800	0.0014	-0.0071		ΔF_3 (Hz)	10.8565	0.0023	-0.0150
	ΔP_{tie12} (p.u)	26.9384	0.0018	-0.0051		ΔP_{tie12} (p.u)	14.5142	0.0015	-0.0079
	ΔP_{tie23} (p.u)	29.2951	0.0023	-0.0023		ΔP_{tie23} (p.u)	21.5476	0.0032	-0.0032
	ΔP_{tie31} (p.u)	28.3064	0.0034	-0.0034		ΔP_{tie31} (p.u)	7.9214	3.0962×10^{-4}	-0.0048

Table 8 Settings of T2FPD + 2DOFPID controller obtained from different optimizers with RLD

Controller	Gains	Area-1	Area-2	Area-3	ITAE	Controller	Gains	Area-1	Area-2	Area-3	ITAE
T2FPD + 2DOFPID	K_P	1.3695	0.0083	0.2065	11.3028	T1FPD + 2DOFPID	K_P	0.2050	0.00054	1.8691	111.9384
	K_D	2	2	0.1478			K_D	0.1748	0.0424	1.9124	
	K_{PP}	1.9993	0.0083	0.2545			K_{PP}	0.0990	2	0.0567	
	b_i	0.0107	0.0183	1.9961			b_i	0.0597	0.0418	0.4324	
	c_i	2	0.1391	0.2804			c_i	2	1.2885	0.0442	
	k_p	0.1173	2	0.0531			k_p	0.0519	0.0211	0.0049	
	k_d	0.2311	0.0887	0.0688			k_d	0.0602	0.2548	2	
	k_i	0.7433	0.0295	0.0011			k_i	0.3241	0.0417	0.00077	
T2FID + 2DOFPID	K_P	0.1385	2	0.0533	65.9403	T2FID + PD	K_P	0.2545	0.0014	0.0144	96.6070
	K_D	0.0656	0.6238	0.1643			K_D	0.3121	2	1.9030	
	K_i	2	0.0012	0.0011			K_i	0.0141	0.0013	0.0025	
	b_i	0.5205	0.0012	0.1039			K_{pp}	0.8018	0.0123	0.8519	
	c_i	0.2214	0.0012	0.0901			K_{dd}	0.3121	2	0.1857	
	k_p	2	1.2261	0.1688		T1FID + PD	K_P	2	0.0777	0.0001	60.1940
	k_d	0.1788	0.1373	0.0981			K_d	2	0.2067	0.0218	
	k_i	0.0531	0.1433	0.0012			K_i	0.0680	0.0001	2	
PID	K_P	0.9578	0.2104	0.7959	33.9306		K_{pp}	0.0001	0.0001	0.2316	
	K_i	2	0.0001	0.0001			K_{dd}	2	0.0360	0.0001	
	K_D	1.9969	0.0048	0.1280							

yield satisfactory control action in the presence of CTD is evident.

5.1.3.3 Effect of plugging in EV EVs contribute toward enhancing grid management infrastructure in the power sector. It is a unique form of distributive energy that can

help in balancing unaccounted supply and demand in any area. Figure 8c shows the responses before and after the addition of EVs to the system using the AOAVOA-tuned T2FPD + 2DOFPID settings given in Table 4. From the decreased undershoots, overshoots, and settling time

Table 9 Statistical results of independent runs

Algorithm	ITAE _{MAX}	ITAE _{MIN}	ITAE _{AVG}	ITAE _{STD}
EO	442.3976	51.6371	11.14215	13.78595
AO	1.21859	0.02493	1.9873	0.6997
AVOA	4.1605	0.2055	3.03514	1.6232
AOAVOA	1.12856	0.02297	0.8193	0.6608

shown in Fig. 8c, it is clear that EVs improve system performance appreciably.

5.1.4 Sensitivity analysis

Since it is difficult to have perfect models of PS components, analyzing the impact of parametric variations on the dynamic response is important. Thus, the goal of this analysis is to determine the robustness of the tuned controller against changes in PS parameters. Thermal parameters in area-1 are changed by $\pm 30\%$ in the studies. The time domain specifications are not significantly affected by parametric modifications in dynamic responses as shown in Fig. 9a and Table 10.

5.2 Bilateral-based scheme

In this case, GENCOs can exchange power with any DISCO. DPM is a representation of the power exchange pact among GENCOs and DISCOs. The DPM used for this scenario is adopted from [82]. For bilateral transactions, participation factors are: $pf_{11} = 0.1$, $pf_{12} = 0.3$, $pf_{13} = 0.6$, $pf_{21} = 0.6$, $pf_{22} = 0.4$, $pf_{31} = 0.6$ and $pf_{32} = 0.4$. Table 11 displays the T2FPD+2DOFPID controller settings produced using various optimization strategies. The load is assumed to be demanded only by DISCOs from its own area GENCOs. The load demand of all DISCOs is assumed to be 0.005 (i.e., $P_{L1} = P_{L2} = P_{L3} = P_{L4} = P_{L5} = P_{L6} = 0.005$ pu). GENCOs essentially generate steady-state power ($\Delta P_{G1} = 0.005$, $\Delta P_{G2} = 0.007$, $\Delta P_{G3} = 0.004$, $\Delta P_{G4} = 0.005$, $\Delta P_{G5} = 0.005$ and $\Delta P_{G6} = 0.004$, $\Delta P_{\text{tie12scheduled}} = 0.001$, $\Delta P_{\text{tie23scheduled}} = 0.001$, and $\Delta P_{\text{tie31scheduled}} = 0$). The GENCO outputs are presented in Fig. 6b whereas the actual tie-line power deviations are shown in Fig. 6c. Moreover, $\Delta P_{\text{tie12scheduled}} = \Delta P_{\text{tie12actual}}$, $\Delta P_{\text{tie31scheduled}} = \Delta P_{\text{tie31actual}}$, and $\Delta P_{\text{tie23scheduled}} = \Delta P_{\text{tie23actual}}$. Hence, $\Delta P_{\text{tie12error}} = \Delta P_{\text{tie23error}} = \Delta P_{\text{tie31error}} = 0$ [82]. The dynamic responses resulting from different optimizers

used to tune the suggested controller are compared in Fig. 9b to vindicate the effectiveness of AOAVOA.

5.3 Contract violation-based scheme.

Contract violations are defined as demanding more electricity from DISCO than was bargained in the agreement. The GENCOs in the same region as the DISCO provide this uncontracted power. Let us assume that DISCO-1 is requesting 0.005 pu of additional power, and thus the overall supply (ΔP_{L1}) in area-1 is the sum of the supplies for DISCO-1, DISCO-2, and is a violation. The total supply of area-2 (ΔP_{L2}) is the result of adding a supply of DISCO-3 and DISCO-4, whereas the total supply of area-3 (ΔP_{L3}) is the result of adding a supply of DISCO-5 and DISCO-6. For the case of contract violation, the values of the DPM matrix and the apfs are similar to those of a bilateral transaction. The overall load demand for area-1 after requesting an extra 0.005 pu of power from DISCO1 is as follows: supply to DISCO-1 & DISCO-2+violation = $0.005 + 0.005 + 0.005 = 0.015$ pu. Because of higher power requirements in area-1, the steady-state generation for area-1 will differ from the bilateral case. $\Delta P_{G1} = 0.005 + (0.005 \times 0.005) = 0.005025$, $\Delta P_{G2} = 0.007 + (0.005 \times 0.005) = 0.007025$. The GENCO outputs are presented in Fig. 6b whereas the actual tie-line power deviations are shown in Fig. 6c. Table 11 displays the T2FPD+2DOFPID controller settings produced using various optimization strategies, while Fig. 9c demonstrates the effectiveness of the proposed scheme through the enhanced dynamic responses.

5.4 Stability and robustness

The Laplace transform of the n th area PS shown in Fig. 10 is [23]:

$$\Delta F_n(s) = G_{pn}(s)G_{cn}(s)U_n(s) + G_D(s)\Delta D_n(s) + G_{\text{tie}}(s)\Delta P_{\text{tie}}(s) \quad (29)$$

Substituting $\Delta D_n(s) = 0$ and $\Delta P_{\text{tie}}(s) = 0$ into (29) yields:

$$\frac{\Delta F_n(s)}{U_n(s)} = G_{pn}(s) \times G_{cn}(s) \quad (30)$$

The loop transfer function for the n th area is given by the above equation. As G_{pn} has nonlinearities such as TDB, TBD, and GRC, it is linearized using a linear analysis toolbox. Using MATLAB/SIMULINK's linear analysis tool, Eq. (30) for area-1 is calculated as:

$$G_{C1}G_{p1} = \frac{143s^6 + 2455s^5 + 9053s^4 + 9109s^3 + 3128s^2 + 257.3s + 2.675}{s^8 + 18.21s^7 + 81.16s^6 + 130s^5 + 90.34s^4 + 26.86s^3 + 2.676s^2 + 0.07716s} \quad (31)$$

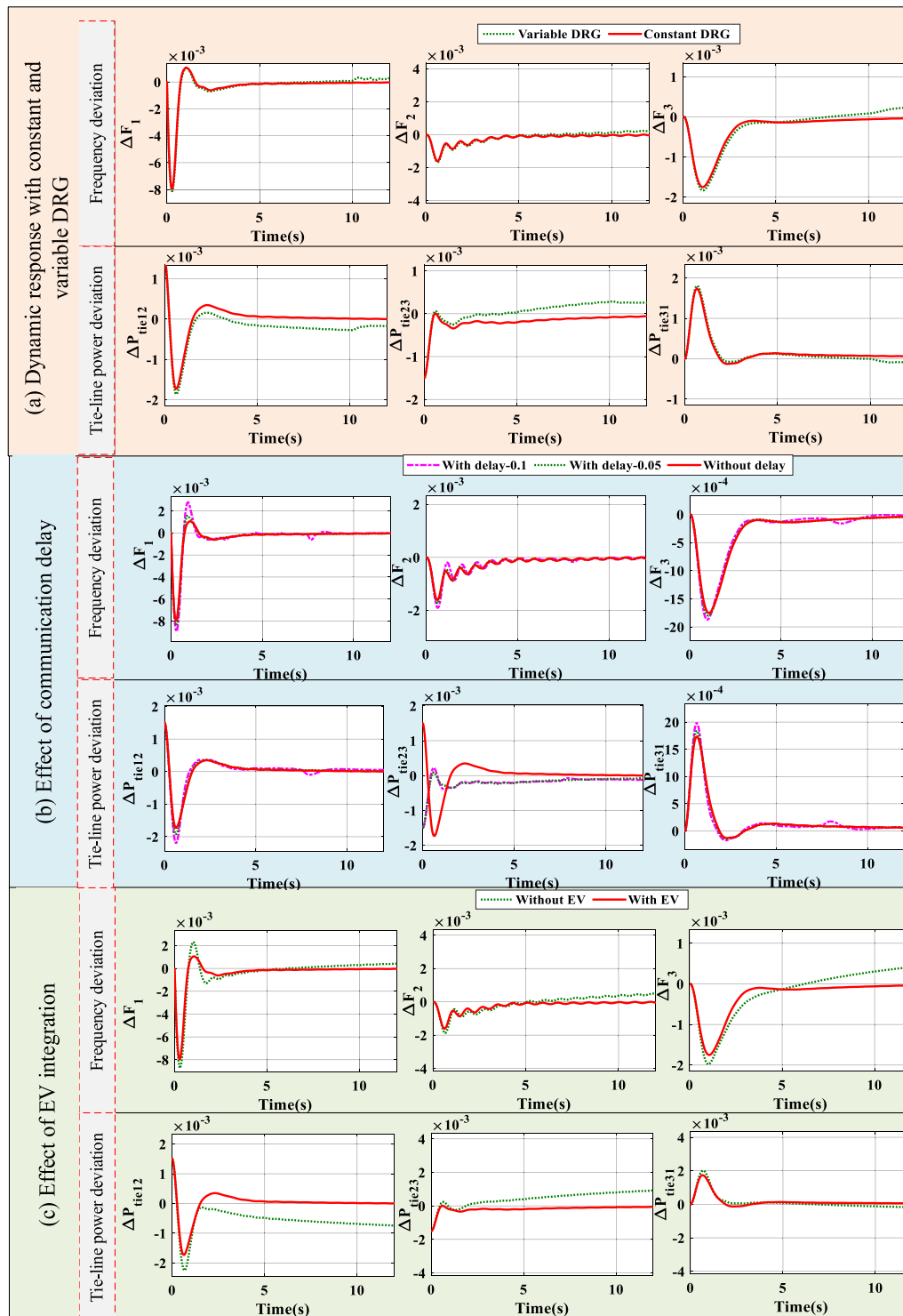


Fig. 8 Dynamic responses of different case studies

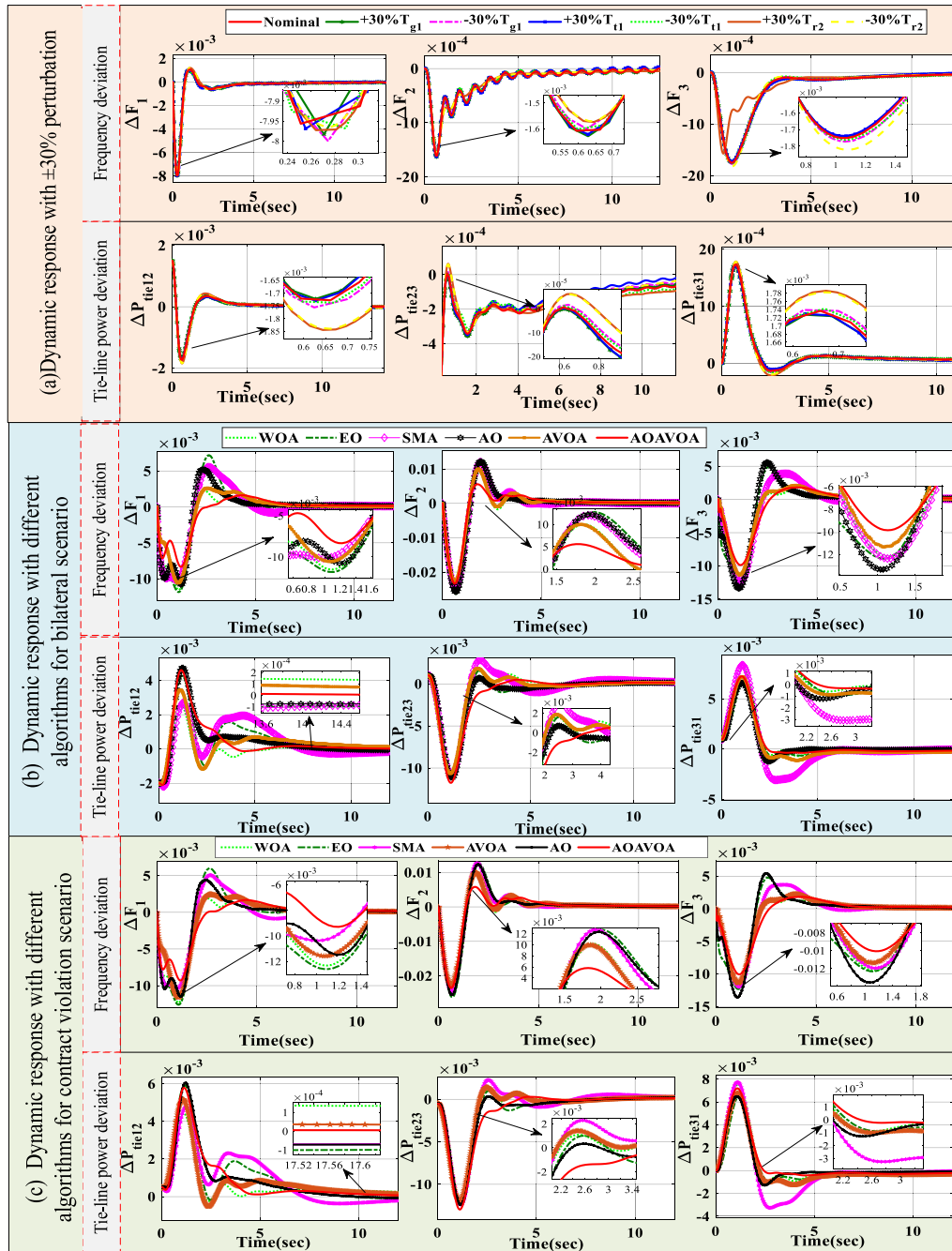


Fig. 9 Dynamic response for **a** $\pm 30\%$ perturbation in thermal parameters in area-1, **b** various optimizers during the bilateral scenario, **c** various optimizers during contract violation

Similar equations for area-2 and 3 are:

$$G_{C2}G_{p2} = \frac{-9.609e - 05s^3 - 0.0005166s^2 + 0.02091s + 0.007024}{s^5 + 15.98s^4 + 44.05s^3 + 6.329s^2 + 0.2083s} \quad (32)$$

$$G_{C3}G_{p3} = \frac{0.0004388s + 0.0009032}{s^4 + 30.05s^3 + 201.5s^2 + 10s} \quad (33)$$

The Bode diagrams of (31), (32), and (33) are shown in Fig. 11. For the robust stability study, the following three scenarios are considered: (1) with G_{C1} , G_{C2} , and G_{C3} (controlled) and without perturbation in PS parameters; (2) with G_{C1} , G_{C2} , and G_{C3} (controlled) and -30% perturbation in PS parameters; and (3) without G_{C1} , G_{C2} , and G_{C3} (uncontrolled) and perturbation in PS parameters.

Table 10 Quantitative performance measures with perturbed thermal parameters

Change % in parameter		+ 30%			− 30%		
Parameter	Signal deviation	$T_s(s)$	MOS	MUS	$T_s(s)$	MOS	MUS
T_{g1}	$\Delta F_1(\text{Hz})$	4.2659	0.0012	− 0.0080	4.5348	0.0012	− 0.0080
	$\Delta F_2(\text{Hz})$	10.0376	− 6.2004* 10^{-7}	− 0.0016	12.6551	7.6008* 10^{-6}	− 0.0016
	$\Delta F_3(\text{Hz})$	10.4244	3.8198* 10^{-6}	− 0.0018	13.4603	1.0998* 10^{-5}	− 0.0018
	$\Delta P_{tie12}(\text{p.u.})$	10.6623	4.3303* 10^{-4}	− 0.0018	7.4649	4.3202* 10^{-4}	− 0.0019
	$\Delta P_{tie23}(\text{p.u.})$	13.2279	4.9364* 10^{-5}	− 0.0015	14.0294	7.4357* 10^{-5}	− 0.0015
	$\Delta P_{tie31}(\text{p.u.})$	12.1055	0.0018	− 0.0018	13.1274	0.0018	− 0.0018
T_{t1}	$\Delta F_1(\text{Hz})$	8.2518	0.0012	− 0.0080	4.0196	0.0012	− 0.0080
	$\Delta F_2(\text{Hz})$	13.0810	5.3550* 10^{-6}	− 0.0016	6.4475	− 3.4467* 10^{-5}	− 0.0016
	$\Delta F_3(\text{Hz})$	13.5399	8.3892* 10^{-6}	− 0.0018	7.0292	− 3.5329* 10^{-5}	− 0.0018
	$\Delta P_{tie12}(\text{p.u.})$	11.0674	4.2616* 10^{-4}	− 0.0018	4.1992	4.3872* 10^{-4}	− 0.0019
	$\Delta P_{tie23}(\text{p.u.})$	14.7153	5.7613* 10^{-5}	− 0.0015	8.9458	6.9997* 10^{-5}	− 0.0015
	$\Delta P_{tie31}(\text{p.u.})$	12.4801	0.0018	− 0.0018	6.2557	0.0018	− 0.0018
T_{r1}	$\Delta F_1(\text{Hz})$	3.6732	0.0012	− 0.0080	11.4743	0.0012	− 0.0080
	$\Delta F_2(\text{Hz})$	7.9805	− 2.6276* 10^{-5}	− 0.0016	15.8649	3.6404* 10^{-5}	− 0.0016
	$\Delta F_3(\text{Hz})$	8.8403	− 2.6452* 10^{-5}	− 0.0018	15.7738	2.9962* 10^{-5}	− 0.0018
	$\Delta P_{tie12}(\text{p.u.})$	6.1326	4.3360* 10^{-4}	− 0.0018	12.6233	4.1637* 10^{-4}	− 0.0018
	$\Delta P_{tie23}(\text{p.u.})$	10.2592	6.2876* 10^{-5}	− 0.0015	19.9326	6.7439* 10^{-5}	− 0.0015
	$\Delta P_{tie31}(\text{p.u.})$	7.9154	0.0018	− 0.0018	15.7498	1.3557* 10^{-4}	− 0.0018

Table 11 Settings of proposed T2FPD + 2DOFPID controller obtained from different optimizers for bilateral/contract violation

Optimization	Gains	Area-1	Area-2	Area-3	Optimization	Gains	Area-1	Area-2	Area-3
AOAVOA	K_P	1.9898	1.8600	0.1279	SMA	K_P	0.2914	0.0101	1.6845
	K_D	0.2593	1.9588	2		K_D	0.0102	0.4528	1.3782
	K_{PP}	1.9676	0.1833	0.3583		K_{PP}	0.1466	0.6270	0.6605
	b_i	0.1521	0.0255	1.9172		b_i	0.2779	1.2606	1.0158
	c_i	0.2112	0.0734	0.0789		c_i	0.6693	1.5276	0.4695
	k_p	1.9588	0.4784	2		k_p	2	0.1054	1.9980
	k_d	1.9792	0.6897	1.9898		k_d	1.6429	0.0262	1.3585
	k_i	1.8914	1.9996	1.9792		k_i	1.5505	1.8830	1.2440
AO	K_P	0.5752	1.9583	1.4396	EO	K_P	1.3543	1.6042	1.2240
	K_D	0.5414	0.0840	0.0320		K_D	0.7975	0.0868	0.3954
	K_{PP}	2	0.1809	1.9796		K_{PP}	1.1770	0.1009	0.1656
	b_i	1.7505	1.9894	0.1427		b_i	0.0221	1.2061	1.4927
	c_i	0.0569	2	0.001		c_i	0.3315	0.0717	0.4336
	k_p	1.9894	0.0143	0.0542		k_p	1.4473	0.0678	0.9080
	k_d	0.1938	0.2090	0.5135		k_d	1.2782	0.3376	0.1986
	k_i	1.9796	1.5647	1.9690		k_i	1.7787	1.0539	1.4847
AVOA	K_P	1.9287	0.0012	1.9331	WOA	K_P	0.8184	0.1920	0.6735
	K_D	1.4025	1.9328	1.9332		K_D	1.7164	0.9697	1.7164
	K_{PP}	1.9323	0.0012	1.7692		K_{PP}	1.0918	0.1608	1.3366
	b_i	1.9330	1.9271	1.5591		b_i	1.7164	0.6188	1.1132
	c_i	1.9248	1.9313	1.9314		c_i	1.1810	1.7164	1.1296
	k_p	0.1929	0.2744	1.9272		k_p	1.7130	0.4624	1.7164
	k_d	1.4360	0.2052	1.9338		k_d	0.2068	0.0914	1.7164
	k_i	1.9312	1.6405	1.9335		k_i	0.6581	1.7164	1.7164

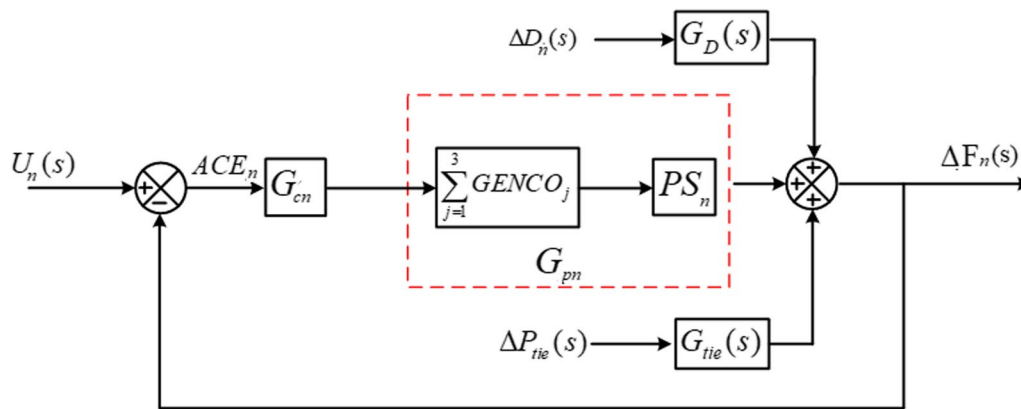


Fig. 10 Generalized block diagram of the i th area in a multi-area PS

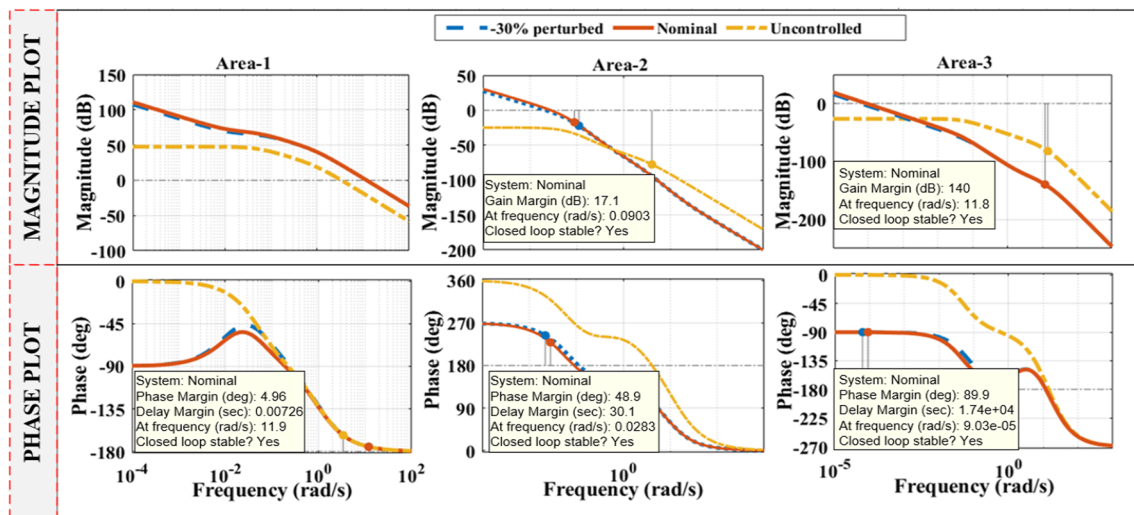


Fig. 11 Bode graphs of loop transfer functions

The stability margins (gain and phase margins: GM_R and PM_R) and crossover frequencies (W_{gc} and W_{pc}) of Fig. 11 are given in Table 12. Figure 11 shows that the considered perturbation in PS parameters does not disturb the system's closed-loop stability. Because the plots for the uncontrolled system do not exceed the 0 dB line, there is no W_{gc} and associated PM_R in Table 12. It is also evident that the proposed controller stabilizes the closed-loop system in all three areas.

5.5 Comparison of AOAVOA-tuned T2FPD + 2DOFPID method with previously reported works.

The performance of the AOAVOA-tuned T2FPD + 2DOF strategy is compared with some contemporary LFC strategies of Parmar et al. [8], Shankar et al. [51], Aryan and

Raja [23], Anand et al. [24], Nayak et al. [6], Prakash and Parida [83] in Table 13 and Fig. 12.

5.5.1 Comparison-1

The PS version employed in [8] is used for the dynamic response comparison-1 shown in Fig. 12(a). It is a two-area deregulated PS. Reference [8] uses a state feedback controller while [51] used the integral secondary controller. In [23], the EO-optimized type-1 Fuzzy FOPI + PIDN strategy is deployed while [24] improves it further by using the AOA-tuned type-2 fuzzy ID + P controller. The proposed controller is responding with a significantly better performance than the other control schemes as seen in Fig. 12a and Table 13.

Table 12 Stability margins and crossover frequencies

Parameter	Area-1			Area-2			Area-3		
	GM_R (dB)	W_{pc} (rad/s)	PM_R (deg)	W_{gc} (rad/s)	GM_R (dB)	W_{pc} (rad/s)	PM_R (deg)	W_{gc} (rad/s)	W_{gc} (rad/s)
Without controller	–	–	17.3	3.39	77.6	4.12	–	14.2	–
With controller									
Nominal	–	–	4.96	11.9	17.1	0.0903	48.9	11.8	9.03×10^{-5}
– 30% Perturbation	–	–	5.07	11.9	22.1	0.113	63.7	11.8	6.32×10^{-5}

Table 13 Performance comparison with published literature

Max deviation	State feedback [8]	I-controller [51]	T1FFOPI + PIDN [23]	T2FID + P [24]	Proposed
Comparison-1					
ΔF_{1max} (Hz)	-0.19680	-0.08885	-0.08503	-0.0839	-0.0864
ΔF_{2max} (Hz)	-0.07160	-0.05726	-0.04823	-0.0452	-0.04323
ΔP_{tie} (p.u)	-0.02511	-0.01922	-0.01635	-0.0153	-0.01418
Max deviation	PID [6]		FPID [6]		Proposed
Comparison-2					
ΔF_{1max} (Hz)	-0.222799		-0.200723		-0.1144
ΔF_{2max} (Hz)	-0.083416		-0.060854		-0.0197
ΔP_{tie} (p.u)	-0.026693		-0.020096		-0.0124
Max deviation	LQR-I [83]		LQR-PI [83]		Proposed
Comparison-3					
ΔF_{1max} (Hz)	-0.01896		-0.017750		-0.008376
ΔF_{2max} (Hz)	-0.01094		-0.009863		-0.007012
ΔP_{tie} (p.u)	-0.00479		-0.004245		-0.006707

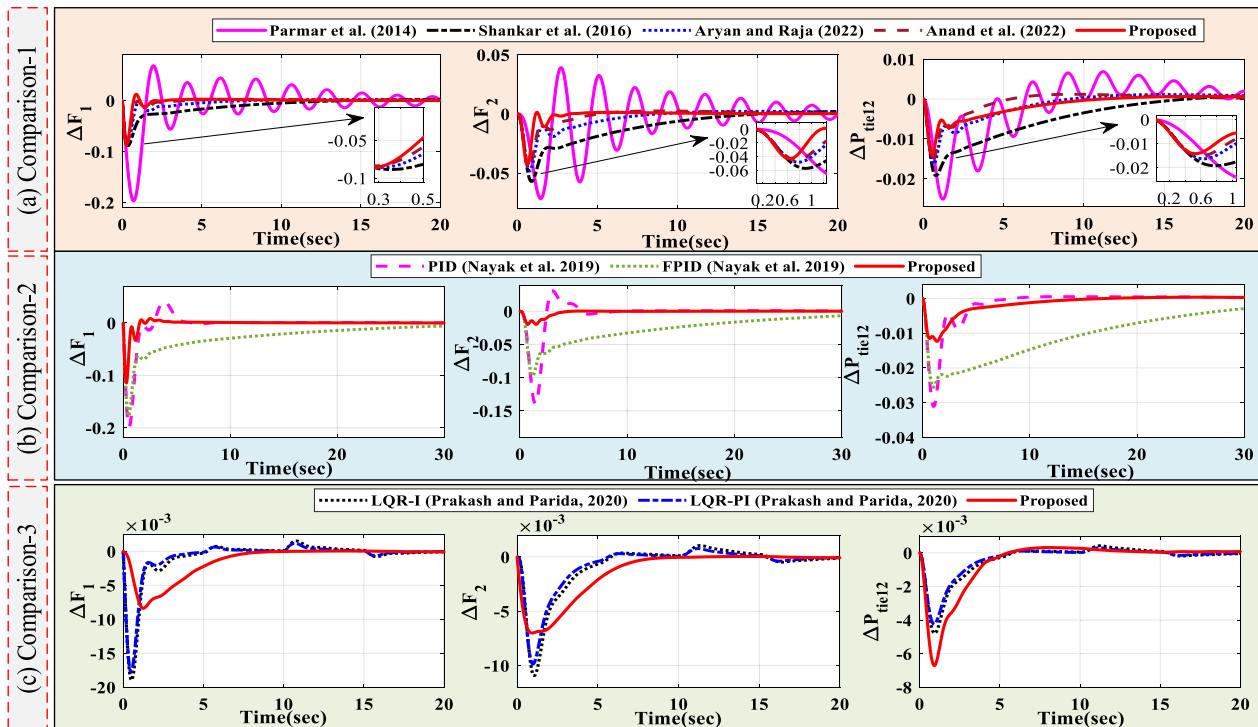


Fig. 12 Comparison of the suggested control scheme with reported strategies

5.5.2 Comparison-2

Reference [6] investigates a two-area, two GENCO (thermal+gas) deregulated PS with modified sine-cosine algorithm (MSCA)-tuned PID and fuzzy PID controllers. The suggested controller delivers much ameliorated dynamic responses to 10% SLD as is evident in Fig. 12b and Table 13.

5.5.3 Comparison-3

In [83], a two-area interconnected PS with renewable integration such as SPV and WTP is investigated, where LQR-based I and PI controllers are designed. The intermittencies of renewables are seen in the dynamic responses to 1% SLD of both LQR-I and LQR-PI schemes in Fig. 12c. The suggested controller on the other hand provides an enhanced and stable response. Also, the maximum frequency deviations are significantly improved with the suggested controller as is evident from Table 13.

6 Conclusion

A novel type-2 fuzzy proportional-derivative bifurcated with a dual degree-of-freedom proportional-integral-derivative (T2FPD+2DOFPID) controller is proposed. This controller is tuned using the proposed hybrid arithmetic optimized African vulture's optimization algorithm (AOAVOA) for a three-area restructured

power system (PS). Integration of time-weighted absolute error (ITAE) is chosen as the cost function. The PS chosen for this study includes thermal, electric vehicle (EV), and distributed renewable generation (DRG) sources in area-1. Thermal and gas units are considered in area-2 whereas thermal-geothermal configuration is considered in area-3. The advantage of the suggested AOAVOA-tuned T2FPD+2DOFPID controller is recognized by conducting comparative studies with other controller configurations and optimizers (amid step and random load disturbances). The effect of EV discharge on system dynamics is also studied. A statistical comparison of AOAVOA, arithmetic optimizer (AO), and African vulture's optimization algorithm (AVOA) is also performed with five independent runs. It is discovered that the maximum ITAE is 1.129 for AOAVOA, 1.219 for AO, and 4.161 for AVOA, the minimum ITAE is 0.023 for AOAVOA, 0.025 for AO and 0.206 for AVOA, the average ITAE is 0.819 for AOAVOA, 1.987 for AO and 3.035 for AVOA, the standard deviation is 0.661 for AOAVOA, 0.700 for AO and 1.623 for AVOA. Finally, the proposed scheme's outcomes are evaluated against a few recently published works, and a robust-stability study is also performed. The maximum frequency deviation in area-1 is mitigated by 2.89% while that of area-2 is mitigated by over 4.55% and tie-line power deviation is mitigated by

7.89% as compared to the recent works. The present work can be further enhanced with proper load forecasting with the integration of renewable sources in all control areas.

Abbreviations

FOF-PID	Fractional Order Fuzzy-Proportional Integral Derivative
FPIDN-FOI	Fuzzy Proportional Integral Derivative with filter-Fractional Order Integral
MPC	Model Predictive Control
FFOPI-FOPD	Fuzzy Fractional Order Proportional Integral-Fractional Order Proportional Derivative
FOD	Fractional Order Derivative
2-DOF-PIDN	2-Degree freedom-PID with filter
IDN-FOPD	Integral Derivative with Filter-Fractional Order Proportional Derivative
IT2FPID	Interval Type-2 Fuzzy PID
CC-2-DOF (PI)-PDF	Cascaded 2-DOF (PI)-proportional derivative with filter
FFOPI + PIDN	Fuzzy Fractional Order PI + PIDN
CFPD ^u F-PI	Cascade Fuzzy Fractional Order Proportional Derivative with Filter-PI
T2FID + I	Type-2 Fuzzy Integral Derivative + Integral
STFPI	Self-tuning Fuzzy PI
TID	Tilt Integral Derivative
T2FID + PD	T2FID + Proportional Derivative
OHS	Opposition-based Harmony Search
BFOA	Bacterial Foraging Optimization Algorithm
ICA	Imperialist Competitive Algorithm
MOOF	Multi-objective Optimization Framework
MSCA	Modified Sine Cosine Algorithm
VPLA	Volleyball Premier League Algorithm
WO	Whale Optimizer
ISA	Interactive Search Algorithm
SA	Sunflower Algorithm
MEO	Modified Equilibrium Optimization
OVPLA	Opposition-based Volleyball Premier League Algorithm
QOEO	Quasi-opposition-based Equilibrium Optimizer
SMA	Slime Mold Algorithm
AO	Arithmetic Optimizer
MGWO-CSA	Modified Grey Wolf Optimization-Cuckoo Search Algorithm
SMES	Superconducting Magnetic Energy Storage
SSA	Salp Swarm Algorithm
WTS	Wind Turbine System
BESSs	Battery Energy Storage Systems
HPWHs	Heat Pump Water Heaters
HESS	Hybrid Energy Storage System
RFB	Redox Flow Battery
HAE FC	Hydrogen Aqua Equalizer Fuel Cells
SSGT	Single Shaft Gas Turbine
SP	Solar Panel
TD	Time Delay
DRG	Distributed Renewable Generation
TBD	Thermo Boiler Dynamics
TDB	Thermal Governor Dead-band
GRC	Generating Rate Constraint
ITAE	Integrated Time Absolute Error
ITSE	Integrated Time Squared Error
ISE	Integrated Squared Error

Acknowledgements

The authors would like to sincerely acknowledge the valuable time devoted by the Reviewers and the Editor-in-Chief to give suggestions to improve the quality of this work.

Authors' information

Nisha Kumari received her B.Tech. degree in electrical and electronics engineering from Nalanda college of engineering Chandi, Nalanda, India and Master's degree from National Institute of Technology, Patna in 2018 and 2022.

She is currently working towards her Ph.D. in control system with the Indian Institute of Technology (Indian School of Mines), Dhanbad, India. Her research interests include load frequency control, type-2 fuzzy control, branched controller, renewable energy, electric vehicles, and optimization. She has authored some peer-reviewed papers in international conference and reputed journals.

Pulakraj Aryan (Graduate Student Member, IEEE) received the bachelor's degree in electrical and electronics engineering from Birla Institute of Technology, Mesra, Ranchi, India in 2016 and Master's degree from National Institute of Technology, Patna, India in 2020. He is currently working towards the Ph.D. degree in control systems with the National Institute of Technology Patna, India. His current research focuses on optimal control strategies for industrial processes. He has authored several book chapters and has more than 15 publications in peer-reviewed international conference proceedings and reputed journals.

G. Lloyds Raja (Member, IEEE and IFAC-ACDOS) received his Bachelors (in Electronics and Communication Engineering) and Master's (in Embedded System Technologies) degrees from Anna University in 2009 and 2011, respectively. He was awarded Ph.D. from the Electrical Engineering Department of Indian Institute of Technology Patna in 2018. While serving as an Assistant Professor at Kalinga Institute of Industrial Technology (between 2017 and 2020), he visited the department of Automation at Shanghai Jiao Tong University (China) for a short duration as a postdoctoral researcher. Since 2020, he is with the Electrical Engineering Department of National Institute of Technology Patna where he serves as an Assistant Professor. His current research interests include chemical process control, advanced load frequency control strategies, adaptive control and applications of meta-heuristic optimization techniques for controller tuning. He has edited two books on control engineering, authored several book chapters and has more than 40 publications in peer-reviewed international conference proceedings and reputed journals.

Yogendra Arya (Senior Member, IEEE) received his A.M.I.E. in Electrical Engineering from The Institution of Engineers (India), in 2008, M.Tech. (Instrumentation & Control) from Deenbandhu Chhotu Ram University of Science and Technology, Murthal, Haryana, India, in 2010 and Ph.D. from Delhi Technological University, Delhi, India in 2018. Currently, he is working as Associate Professor with J.C. Bose University of Science & Technology, YMCA, Faridabad, India. He has published several research papers and served as the member of editorial board in various reputed journals. He was awarded best associate editor award for 2021 and 2022 by Journal of Electrical Engineering & Technology (SCIE Journal published by Springer). He was placed in "Top 2% of Researchers in the World" list published by Stanford University, USA for 2020, 2021 and 2022. His research interests include AGC/LFC of conventional/restructured power systems.

Author contributions

NK: Formal analysis; writing—original draft. PA: Investigation; resources; software; presentation. GLR: Conceptualization; data curation; supervision; writing—review and editing. YA: Validation; writing—review and editing.

Funding

Not applicable.

Availability of data and materials

The authors confirm that data and materials that support the results or analyses presented in this paper are freely available upon request.

Declarations

Competing interests

The authors declare that they have no competing interests.

Received: 12 January 2023 Accepted: 22 August 2023

Published online: 22 September 2023

References

1. Saha, A., & Saikia, L. C. (2019). Load frequency control of a wind-thermal-split shaft gas turbine-based restructured power system integrating

- FACTS and energy storage devices. *International Transactions on Electrical Energy Systems*, 29(3), 1–19.
2. Ranjan, M., & Shankar, R. (2022). A literature survey on load frequency control considering renewable energy integration in power system: Recent trends and future prospects. *Journal of Energy Storage*, 45, 103717.
 3. Fathy, A., & Alharbi, A. G. (2021). Recent approach based movable damped wave algorithm for designing fractional-order PID load frequency control installed in multi-interconnected plants with renewable energy. *IEEE Access*, 9, 71072–71089.
 4. Murali, S., Prakash, A., & Shankar, R. (2019). LFC of multi area power system with electric vehicle using VPL optimized controller. In *1st International conference on power electronics applications and technology in present energy scenario*, 2(c), 4–9.
 5. Farooq, Z., Rahman, A., & Lone, S. A. (2021). System dynamics and control of EV incorporated deregulated power system using MBO-optimized cascaded ID-PD controller. *International Transactions on Electrical Energy Systems*, 31(11), 1–22.
 6. Nayak, N., Mishra, S., Sharma, D., & Sahu, B. K. (2019). Application of modified sine cosine algorithm to optimally design PID/fuzzy-PID controllers to deal with AGC issues in deregulated power system. *IET Generation, Transmission and Distribution*, 13(12), 2474–2487.
 7. Donde, V., Pai, M. A., & Hiskens, I. A. (2001). Simulation and optimization in an AGC system after deregulation. *IEEE Transactions on Power Systems*, 16(3), 481–489.
 8. Parmar, K. P. S., Majhi, S., & Kothari, D. P. (2014). LFC of an interconnected power system with multi-source power generation in deregulated power environment. *International Journal of Electrical Power and Energy Systems*, 57, 277–286.
 9. Shankar, R., Bhushan, R., & Chatterjee, K. (2016). Small-signal stability analysis for two-area interconnected power system with load frequency controller in coordination with FACTS and energy storage device. *Ain Shams Engineering Journal*, 7(2), 603–612.
 10. Arya, Y., & Kumar, N. (2017). BFOA-scaled fractional order fuzzy PID controller applied to AGC of multi-area multi-source electric power generating systems. *Swarm and Evolutionary Computation*, 32, 202–218.
 11. Arya, Y. (2018). Improvement in automatic generation control of two-area electric power systems via a new fuzzy aided optimal PIDN-FOI controller. *ISA Transactions*, 80, 475–490.
 12. Magdy, G., Shabib, G., Elbaset, A. A., & Mitani, Y. (2018). Optimized coordinated control of LFC and SMES to enhance frequency stability of a real multi-source power system considering high renewable energy penetration. *Protection and Control of Modern Power Systems*, 3(1), 1–15.
 13. Pahasa, J., & Ngamroo, I. (2014). Coordinated control of wind turbine blade pitch angle and PHEVs using MPCs for load frequency control of microgrid. *IEEE Systems Journal*, 10(1), 97–105.
 14. Arya, Y. (2019). A new optimized fuzzy FOPI-FOPD controller for automatic generation control of electric power systems. *Journal of the Franklin Institute*, 356(11), 5611–5629.
 15. Pappachen, A., & Fathima, A. P. (2019). Impact of SMES–TCSC combination in a multi-area deregulated power system with GA-based PI controller. *Journal of Control, Automation and Electrical Systems*, 30(6), 1069–1081.
 16. Raj, U., & Shankar, R. (2020). Deregulated automatic generation control using novel opposition-based interactive search algorithm cascade controller including distributed generation and electric vehicle. *Iranian Journal of Science and Technology: Transactions of Electrical Engineering*, 44(3), 1233–1251.
 17. Prakash, A., Kumar, K., & Parida, S. K. (2020). PIDF (1 + FOD) controller for load frequency control with SSSC and AC–DC tie-line in deregulated environment. *IET Generation, Transmission & Distribution*, 14(14), 2751–2762.
 18. Nayak, P. C., Nayak, B. P., Prusty, R. C., & Panda, S. (2021). Sunflower optimization based fractional order fuzzy PID controller for frequency regulation of solar-wind integrated power system with hydrogen aqua equalizer-fuel cell unit. *Energy Sources, Part A: Recovery, Utilization and Environmental Effects*, 00(00), 1–19.
 19. Khadanga, R. K., Kumar, A., & Panda, S. (2021). Frequency control in hybrid distributed power systems via type-2 fuzzy PID controller. *IET Renewable Power Generation*, 15(8), 1706–1723.
 20. Oshnoei, A., Kheradmandi, M., Blaabjerg, F., Hatziargyriou, N. D., Muyeen, S. M., & Anvari-Moghaddam, A. (2022). Coordinated control scheme for provision of frequency regulation service by virtual power plants. *Applied Energy*, 325, 119734.
 21. Sharma, M., Saxena, S., Prakash, S., & Dhundhara, S. (2022). Environmental Effects Frequency stabilization in sustainable energy sources integrated power systems using novel cascade noninteger fuzzy controller. *Energy Sources, Part A: Recovery, Utilization, and Environmental Effects*, 44(3), 6213–6235.
 22. Murali, S., & Shankar, R. (2022). Optimal CC-2DOF(PI)-PDF controller for LFC of restructured multi-area power system with IES-based modified HVDC tie-line and electric vehicles. *Engineering Science and Technology, an International Journal*, 32, 101058.
 23. Aryan, P., & Raja, G. L. (2022). Design and analysis of novel QOEO optimized parallel fuzzy FOPI-PIDN controller for restructured AGC with HVDC and PEV. *Iranian Journal of Science and Technology: Transactions of Electrical Engineering*, 46(2), 565–587.
 24. Anand, A., Aryan, P., Kumari, N., & Raja, G. L. (2022). Type-2 fuzzy-based branched controller tuned using arithmetic optimizer for load frequency control. *Energy Sources, Part A: Recovery, Utilization and Environmental Effects*, 44(2), 4575–4596.
 25. Padhi, J. R., Debnath, M. K., & Kar, S. K. (2022). Self-tuning Fuzzy-PI controller for load frequency control analysis with the integration of wind energy. *Energy Sources, Part A: Recovery, Utilization and Environmental Effects*, 44(1), 613–631.
 26. Khadanga, R. K., Kumar, A., & Panda, S. (2022). A modified Grey Wolf Optimization with Cuckoo Search Algorithm for load frequency controller design of hybrid power system. *Applied Soft Computing*, 124, 109011.
 27. Çelik, E., Öztürk, N., & Houssein, E. H. (2022). Influence of energy storage device on load frequency control of an interconnected dual-area thermal and solar photovoltaic power system. *Neural Computing and Applications*, 34(22), 20083–20099.
 28. Kumari, N., Aryan, P., & Raja, G. L. (2022). Optimal type-2 fuzzy based secondary control strategy for three-area hybrid power system integrating renewable sources under various deregulated market scenarios. *SETA-D-22-03247*. <https://doi.org/10.2139/ssrn.4163795>.
 29. Deepak, M., & Abraham, R. J. (2015). Load following in a deregulated power system with Thyristor Controlled Series Compensator. *International Journal of Electrical Power and Energy Systems*, 65, 136–145.
 30. Shankar, R., Pradhan, S. R., Chatterjee, K., & Mandal, R. (2017). A comprehensive state of the art literature survey on LFC mechanism for power system. *Renewable and Sustainable Energy Reviews*, 76, 1185–1207.
 31. Saxena, A., & Shankar, R. (2022). Improved load frequency control considering dynamic demand regulated power system integrating renewable sources and hybrid energy storage system. *Sustainable Energy Technologies and Assessments*, 52, 102245.
 32. Das, S., Datta, S., & Saikia, L. C. (2021). Load frequency control of a multi-source multi-area thermal system including biogas–solar thermal along with pumped hydro energy storage system using MBA-optimized 3DOF-TIDN controller. *International Transactions on Electrical Energy Systems*, 31(12), e13165.
 33. Efe, M. Ö. (2011). Fractional order systems in industrial automation: A survey. *IEEE Transactions on Industrial Informatics*, 7(4), 582–591.
 34. Sahu, R. K., Panda, S., Biswal, A., & Sekhar, G. C. (2016). Design and analysis of tilt integral derivative controller with filter for load frequency control of multi-area interconnected power systems. *ISA Transactions*, 61, 251–264.
 35. Chen, X., Lin, J., Liu, F., & Song, Y. (2019). Optimal control of AGC systems considering non-Gaussian wind power uncertainty. *IEEE Transactions on Power Systems*, 34(4), 2730–2743.
 36. Arya, Y. (2020). A novel CFFOPI-FOPID controller for AGC performance enhancement of single and multi-area electric power systems. *ISA Transactions*, 100, 126–135.
 37. Ramesh, M., Yadav, A. K., & Pathak, P. K. (2021). An extensive review on load frequency control of solar-wind based hybrid renewable energy systems. *Energy Sources, Part A: Recovery, Utilization and Environmental Effects*, 00(00), 1–25. <https://doi.org/10.1080/15567036.2021.1931564>
 38. Dash, P., Saikia, L. C., & Sinha, N. (2016). Flower pollination algorithm optimized PI-PD cascade controller in automatic generation control of a multi-area power system. *International Journal of Electrical Power and Energy Systems*, 82, 19–28.
 39. Aftab, A., & Luan, X. (2022). A fuzzy-PID series feedback self-tuned adaptive control of reactor power using nonlinear multipoint kinetic model

- under reference tracking and disturbance rejection. *Annals of Nuclear Energy*, 166, 108696.
40. Mishra, S., Prusty, U. C., Prusty, R. C., & Panda, S. (2021). Novel load frequency control scheme for hybrid power systems employing interline power flow controller and redox flow battery. *Energy Sources, Part A: Recovery, Utilization and Environmental Effects*, 00(00), 1–19. <https://doi.org/10.1080/15567036.2021.1986174>
 41. Prusty, U. C., Nayak, P. C., Prusty, R. C., & Panda, S. (2022). An improved moth swarm algorithm based fractional order type-2 fuzzy PID controller for frequency regulation of microgrid system. *Energy Sources, Part A: Recovery, Utilization and Environmental Effects*, 00(00), 1–23. <https://doi.org/10.1080/15567036.2022.2038735>
 42. Liu, X., Zhang, Y., & Lee, K. Y. (2017). Coordinated distributed MPC for load frequency control of power system with wind farms. *IEEE Transactions on Industrial Electronics*, 64(6), 5140–5150.
 43. Zhu, J., Cui, X., & Ni, W. (2022). Model predictive control based control strategy for battery energy storage system integrated power plant meeting deep load peak shaving demand. *Journal of Energy Storage*, 46, 103811.
 44. Sharma, P., Mishra, A., Saxena, A., & Shankar, R. (2021). A novel hybridized fuzzy PI-LADRC based improved frequency regulation for restructured power system integrating renewable energy and electric vehicles. *IEEE Access*, 9, 7597–7617.
 45. Mu, C., Tang, Y., & He, H. (2017). Improved sliding mode design for load frequency control of power system integrated an adaptive learning strategy. *IEEE Transactions on Industrial Electronics*, 64(8), 6742–6751.
 46. Mahapatra, A. K., Samal, P., Mohapatra, S., Sahu, P. C., & Panda, S. (2021). Analysis of Gaussian fuzzy logic-sliding model control and flexible AC transmission systems controllers for automatic generation control of hybrid power system under chaotic-water cycle algorithm approach. *International Transactions on Electrical Energy Systems*, 31(12), e13163.
 47. Bhagat, S. K., Saikia, L. C., Raju, D. K., Babu, N. R., Ramoji, S. K., Dekaraja, B., & Behra, M. K. (2021). Maiden application of hybrid particle swarm optimization with genetic algorithm in AGC studies considering optimized TIDN controller. In *Modeling, simulation and optimization* (pp. 335–346). Springer.
 48. Han, J., Solanki, S. K., & Solanki, J. (2013). Coordinated predictive control of a wind/battery microgrid system. *IEEE Journal of Emerging and Selected Topics in Power Electronics*, 1(4), 296–305.
 49. Mohanty, P. K., Sahu, B. K., Pati, T. K., Panda, S., & Kar, S. K. (2016). Design and analysis of fuzzy PID controller with derivative filter for AGC in multi-area interconnected power system. *IET Generation, Transmission and Distribution*, 10(15), 3764–3776.
 50. Nandi, M., Shiva, C. K., & Mukherjee, V. (2017). TCSC based automatic generation control of deregulated power system using quasi-oppositional harmony search algorithm. *Engineering Science and Technology, an International Journal*, 20(4), 1380–1395.
 51. Shankar, R., Chatterjee, K., & Bhushan, R. (2016). Impact of energy storage system on load frequency control for diverse sources of interconnected power system in deregulated power environment. *International Journal of Electrical Power and Energy Systems*, 79, 11–26.
 52. Prakash, A., Murali, S., Shankar, R., & Bhushan, R. (2019). HVDC tie-link modeling for restructured AGC using a novel fractional order cascade controller. *Electric Power Systems Research*, 170, 244–258.
 53. Biswas, S., Roy, P. K., & Chatterjee, K. (2023). Development of MADB of P-I controller using LMI technique in a renewable energy based AGC system and study its application in a deregulated environment including energy storage device. *Optimal Control Applications and Methods*, 44(2), 426–451.
 54. Rahman, A., Saikia, L. C., & Sinha, N. (2017). Automatic generation control of an interconnected two-area hybrid thermal system considering dish-stirling solar thermal and wind turbine system. *Renewable Energy*, 105, 41–54.
 55. Aryan, P., & Raja, G. L. (2022). Restructured LFC scheme with renewables and EV penetration using novel QOEA optimized parallel fuzzy I-PID controller. *IFAC-PapersOnLine*, 55(1), 460–466.
 56. Dhillon, S. S., Lather, J. S., & Marwaha, S. (2015). Multi area load frequency control using particle swarm optimization and fuzzy rules. *Procedia Computer Science*, 57, 460–472.
 57. Guha, D., Roy, P. K., & Banerjee, S. (2020). Whale optimization algorithm applied to load frequency control of a mixed power system considering nonlinearities and PLL dynamics. *Energy Systems*, 11(3), 699–728.
 58. Li, S., Chen, H., Wang, M., Heidari, A. A., & Mirjalili, S. (2020). Slime mould algorithm: A new method for stochastic optimization. *Future Generation Computer Systems*, 111, 300–323.
 59. Yousri, D., Babu, T. S., & Fathy, A. (2020). Recent methodology based Harris Hawks optimizer for designing load frequency control incorporated in multi-interconnected renewable energy plants. *Sustainable Energy, Grids and Networks*, 22, 100352.
 60. Roy, A., Dutta, S., & Roy, P. K. (2015). Load frequency control of interconnected power system using teaching learning based optimization. *International Journal of Energy Optimization and Engineering*, 4(1), 102–117.
 61. Wang, N., Zhang, J., He, Y., Liu, M., Zhang, Y., Chen, C., Gu, Y., & Ren, Y. (2020). Load-frequency control of multi-area power system based on the improved weighted fruit fly optimization algorithm. *Energies*, 13(2), 437.
 62. Garg, H. (2016). A hybrid PSO-GA algorithm for constrained optimization problems. *Applied Mathematics and Computation*, 274, 292–305.
 63. Gheisarnejad, M. (2018). An effective hybrid harmony search and cuckoo optimization algorithm based fuzzy PID controller for load frequency control. *Applied Soft Computing*, 65, 121–138.
 64. Abdollahzadeh, B., Gharehchopogh, F. S., & Mirjalili, S. (2021). African vultures optimization algorithm: A new nature-inspired metaheuristic algorithm for global optimization problems. *Computers and Industrial Engineering*, 158, 107408.
 65. Qin, S., Wang, S., Wang, L., Wang, C., Sun, G., & Zhong, Y. (2020). Multi-objective optimization of cascade blade profile based on reinforcement learning. *Applied Sciences*, 11(1), 106.
 66. Indumathi, G., & Nisha Rani, S. (2022). Hybrid Grey Wolf Optimization with Cuckoo Search-based optimal channel estimation for energy efficient massive multiple input multiple output. *International Journal of Communication Systems*, 35(7), e5106.
 67. Guha, D., Roy, P. K., & Banerjee, S. (2018). Symbiotic organism search algorithm applied to load frequency control of multi-area power system. *Energy Systems*, 9, 439–468.
 68. Gupta, S. K. (2015). *Power system operation control & restructuring*. IK International Publishing House.
 69. Tripathy, S. C., Bhatti, T. S., Jha, C. S., Malik, O. P., & Hope, G. S. (1984). Sampled data automatic generation control analysis with reheat steam turbines and governor dead-band effects. *IEEE Transactions on Power Apparatus and Systems*, 5, 1045–1051.
 70. Haroun, A. G., & Li, Y. Y. (2017). A novel optimized hybrid fuzzy logic intelligent PID controller for an interconnected multi-area power system with physical constraints and boiler dynamics. *ISA Transactions*, 71, 364–379.
 71. Tasnin, W., & Saikia, L. C. (2018). Deregulated AGC of multi-area system incorporating dish-Stirling solar thermal and geothermal power plants using fractional order cascade controller. *International Journal of Electrical Power & Energy Systems*, 101, 60–74.
 72. Rowen, W. I. (1983). Simplified mathematical representations of heavy-duty gas turbines. *Journal of Engineering for Gas Turbines and Power*, 105, 865–869.
 73. Debbarma, S., & Dutta, A. (2016). Utilizing electric vehicles for LFC in restructured power systems using fractional order controller. *IEEE Transactions on Smart Grid*, 8(6), 2554–2564.
 74. Paital, S. R., Ray, P. K., & Mohanty, S. R. (2022). A robust dual interval type-2 fuzzy lead-lag based upfc for stability enhancement using Harris hawks optimization. *ISA Transactions*, 123, 425–442.
 75. Geering, H. P. (1998). *Introduction to fuzzy control*. Measurement and Control Laboratory Swiss Federal Institute of Technology ETH-Zentrum Zurich. <https://doi.org/10.3929/ethz-a-004953512>
 76. Rao, C. S., Nagaraju, S. S., & Raju, P. S. (2009). Automatic generation control of TCPS based hydrothermal system under open market scenario: A fuzzy logic approach. *International Journal of Electrical Power and Energy Systems*, 31(7–8), 315–322.
 77. Abualigah, L., Diabat, A., Mirjalili, S., Abd Elaziz, M., & Gandomi, A. H. (2021). The arithmetic optimization algorithm. *Computer Methods in Applied Mechanics and Engineering*, 376, 113609.
 78. Abualigah, L., & Diabat, A. (2023). Improved multi-core arithmetic optimization algorithm-based ensemble mutation for multidisciplinary applications. *Journal of Intelligent Manufacturing*, 34(4), 1833–1874.
 79. Fan, J., Li, Y., & Wang, T. (2021). An improved African vultures optimization algorithm based on tent chaotic mapping and time-varying mechanism. *PLoS ONE*, 16(11), e0260725.

80. Kaveh, A., Rahmani, P., & Eslamlou, A. D. (2022). An efficient hybrid approach based on Harris Hawks optimization and imperialist competitive algorithm for structural optimization. *Engineering with Computers*, 38(2), 1555–1583.
81. Chen, M., Zhou, Y., & Luo, Q. (2022). An improved arithmetic optimization algorithm for numerical optimization problems. *Mathematics*, 10(12), 2152.
82. Rangi, S., Jain, S., & Arya, Y. (2022). Utilization of energy storage devices with optimal controller for multi-area hydro-hydro power system under deregulated environment. *Sustainable Energy Technologies and Assessments*, 52, 102191.
83. Prakash, A., & Parida, S. K. (2020). LQR based PI controller for load frequency control with distributed generations. In *2020 21st national power systems conference (NPSC)* (pp. 1–5). IEEE.

Submit your manuscript to a SpringerOpen[®] journal and benefit from:

- Convenient online submission
- Rigorous peer review
- Open access: articles freely available online
- High visibility within the field
- Retaining the copyright to your article

Submit your next manuscript at ► [springeropen.com](https://www.springeropen.com)
